Domain-Wall Motion in Materials with Perpendicular Magnetic Anisotropy

Author
D.M.F. Hartmann

Supervisors
E. van der Bijl[1], **R.A. Duine**[1],
R. Lavrijsen[2], **and H.J.M. Swagten**[2]
[1] *Institute for Theoretical Physics, Utrecht University*
[2] *Physics of Nanostructures, Eindhoven University of Technology*

June 18, 2014

Abstract

This Thesis reports on our theoretical and experimental study of the motion of magnetic domains in perpendicular magnetic anisotropy materials. We show that spatial fluctuations of the DMI give rise to a local in plane magnetic field parallel to the domain wall. Our calculations on the atomic scale also point out that the sign and magnitude of the DMI strength is strongly related to the interface structure. This result motivated our experimental study on interface effects which shows that the in-plane magnetic field dependence of the domain wall motion is governed by sample growth parameters. We show that in-plane field effects enter the creep theory in novel ways. Our work leads to new insights concerning the Dzyaloshinskii-Moriya-Interaction, in-plane magnetic fields, creep theory and effects of the conditions under which the studied samples are grown.

Contents

1 Introduction

In 1965 Gordon Moore stated his famous law about the ever increasing capacity of computers. More precisely, Moore stated that the amount of transistors in an integrated circuit doubles every two years [1], resulting in a higher working speed and larger memory capacity. Today we can look back and see that the prophecy of Moore has indeed unfolded and shows no sign of weakening as depicted in figure 1.

However, Moore's law is no law like others in physics: We do not stand from a distance, let nature do its way obeying its laws and observe that indeed by some force in nature somehow the computer capacity keeps on increasing. We are very much involved in this law ourselves, continuously crossing the borders of what is known and expanding the horizon of science and its applications in society. Moore's law is not specifically a law of nature, but one of mankind, and the forces at play are those of desires to understand and develop. It are also exactly these forces that have led me to form this Thesis.

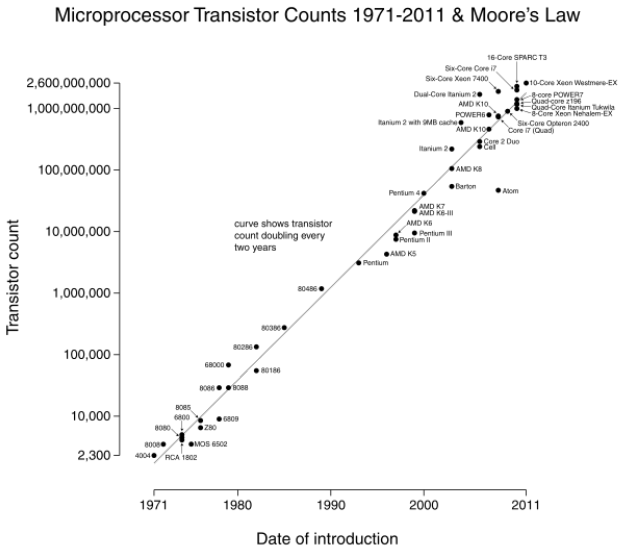

Figure 1: Moore's law in practice. The dots mark the transistor count for integrated circuits at their date of introduction. The line indicates a doubling of the transistor count every two years. Figure taken from [2].

Recently a new type of data storage, to carry on the legacy of Moore's law, was introduced by Stuart Parkin (IBM). This so called *Racetrack Memory* uses the controlled movement of a Domain Wall (DW) in magnetic nanowires to create a nonvolatile data storage device [3]. In this device the nanowire is a racetrack and the magnetic domains are the cars or bits - an up domain corresponds to a 1 and a down domain to a 0 - passing by a read and write device (illustrated in figure 2), driven by an external field or current. By bending the nanowire in a u-shape and using an array of such wires, this type of data storage uses all three dimensions, increasing its storage density. However, for high performance and reliability, DW motion

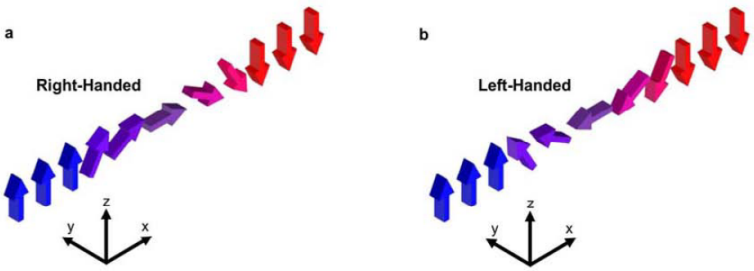

Figure 3: Two chiralities for the DW. The chirality of a DW determines how it is driven by a current. Figure taken from [4].

needs to be well understood. This is one of the reasons why DW motion in ultrathin magnetized metals has become an increasingly popular topic of study.

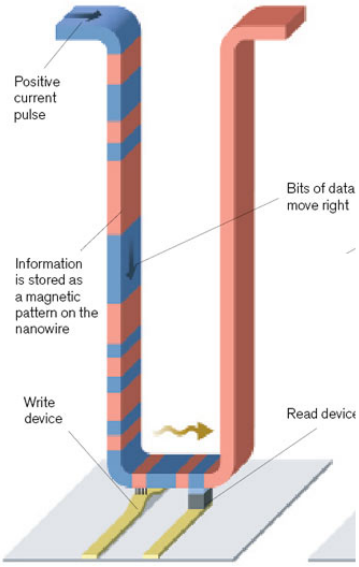

Figure 2: The Racetrack Memory. The blue and red areas mark the different magnetic domains corresponding to bits of data. Figure adapted from [9].

A crucial element for the racetrack memory to work is that all DWs move in the same direction when driven by an external force. A study of the current driving mechanism of DWs shows that coherent motion occurs when all DWs are chiral, *i.e.* they turn in the same sense [4, 5, 6, 7]. In figure 3 two types of chiralities are illustrated for a certain type of DW. As discussed in literature and as we will also show in this Thesis the Dzyaloshinskii-Moriya-Interaction (DMI) makes one specific turning sense energetically favorable above others, thereby insuring coherent DW motion in systems where DMI is present [4, 5, 6, 7]. Understanding the origin of the DMI, its effect on the motion of DWs and how it can be tuned and measured is therefore of crucial importance. As shown in literature and also discussed in this thesis, the DMI acts as a local in-plane (IP) magnetic field perpendicular to the domain wall [4, 5, 6, 7, 8]. So, to measure the DMI and its effect on DW motion the IP field dependence of the motion of a field driven DW is studied.

However, the motion of DWs itself is a long studied topic, still in development today. In 1998 Lemerle *et al.* proposed to use the phenomenological theory of creep to describe the thermally assisted motion of DWs in dis-

ordered systems with small external driving forces [10]. This creep theory suggest an exponential dependence of the following form:

$$\ln(v) \propto -\frac{U_c}{k_B T}\left(\frac{f_c}{f}\right)^{\mu}, \tag{1}$$

where U_c is an energy scaling, k_B the Boltzmann constant, f the driving force with f_c the critical force at which the DW depins at $T = 0$K and μ the creep exponent which classifies the universality class and depends on the type of disorder and dimensionality of the material. In numerous studies equation 1 has been checked and confirmed for simplified cases, *i.e.* one- or two-dimensional perpendicular magnetic anisotropy (PMA) systems with only an out-of-plane (OOP) magnetic field as the driving force [10, 11, 12, 13]. A good understanding how IP fields and the DMI enter this creep theory may be used to accurately measure the DMI strength.

In this Thesis the DMI and IP field effects on DW motion are elaborately studied. Experimental research reported on in this Thesis has led to an extensive revisit of this creep theory. The experiment was done to gain insight in how interface properties of the metallic multilayered structures studied affect the DMI. In this research symmetric samples of the same size and thickness are grown under different circumstances, resulting in a variation in the interface roughness. Next, the IP field dependence of the velocity is determined for each sample as well as other sample properties, such as the anisotropy and magnetic moment. As will be described in this Thesis the results are in disagreement with other studies and have led to an interesting discussion and increased interest in the creep theory.

The remainder of this Thesis is organized as follows. First, the theoretical background of DW dynamics is explained in section 2. Then, based on the theory and proposed origin of the DMI, in section 3 we study how the roughness of the interface between the metallic layers of the studied material influences the DMI and how a DMI that spatially fluctuates affects the DW dynamics. Motivated by our experimental research, we discuss in section 4 an extension of creep theory with respect to IP magnetic field and DMI. Next, this theory is used to form one- and two-dimensional models of magnetic domain expansion in section 5. These models will be used to compare the theory with experimental observations. After the theoretical work, in section 6 the experiment and its results are described. The results and theory are compared and interpreted in section 7. This leads to the discussion, conclusion and lastly, the outlook given in section 8.

2 Theoretical Background

In this Thesis it is assumed that the reader has basic knowledge about electromagnetism, quantum mechanics, classical mechanics, statistical physics and classical field theory. Standard references are [14, 15, 16, 17, 18].

2.1 System Description

The type of system studied in this Thesis is a one-dimensional (1D) or two-dimensional (2D) system corresponding to a nanowire or surface, respectively, composed of ultrathin metallic layers of which at least one is ferromagnetic. The ferromagnetic layer is sandwiched between non-magnetic layers. The typical thicknesses of these layers are on the order of nanometers and often the ferromagnetic layer is two to four layers of atoms thick.

In the 1D systems we define our Cartesian coordinate system with the x-axis along the length of the nanostrip and the z-axis perpendicular to the plane of the layers. For the 2D systems we define the Cartesian x-y plane to be parallel to the plane of the layers and the x-axis parallel to the applied IP magnetic field. In figure 4 the systems that are studied are illustrated schematically.

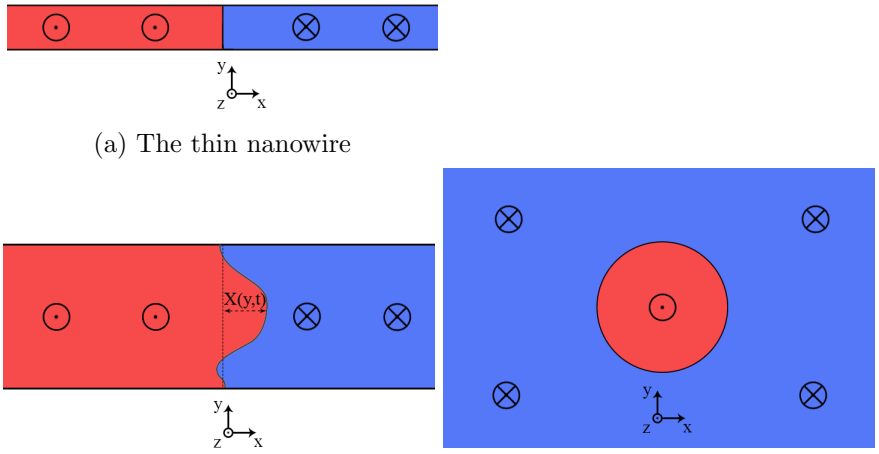

(a) The thin nanowire

(b) The wide nanowire

(c) The 2D system

Figure 4: The studied systems. The vector markings indicate the direction of the magnetization in the ferromagnetic layer.

2.1.1 Perpendicular Magnetic Anisotropy

The materials used give the system a perpendicular magnetic anisotropy (PMA), *i.e.* the magnetic moment of the ferromagnetic layer is always pointing in a direction perpendicular to the plane of nanowire or surface

(except locally at the position of the DW as we see in figure 7). The PMA in the ferromagnetic ultrathin layer arises due to hybridization processes between the electron shells of the ferromagnetic and nonmagnetic layers. This effect is called magnetocrystalline anisotropy and occurs on the interface, so by making ultrathin layers the interface effects, *i.e.* the magnetocrystalline anisotropy, dominate over bulk effects, *i.e.* shape anisotropy, as illustrated in figure 5. For more details on this process we refer to [19, 20].

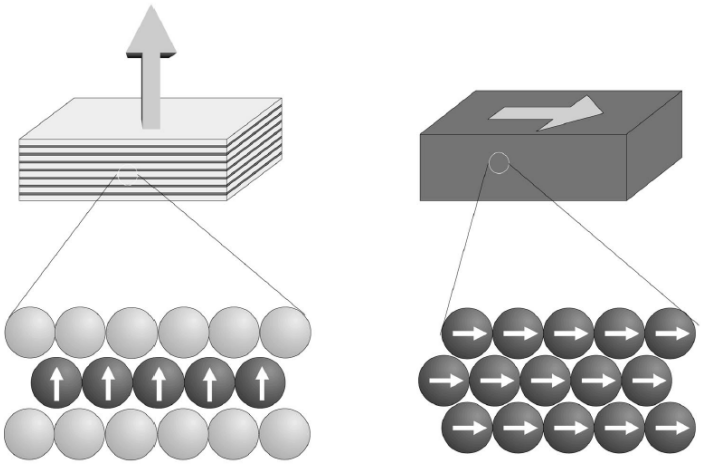

Figure 5: When the ferromagnetic layers are thin enough, interface effects become more important than bulk effects. SO magnetocrystalline anisotropy then dominates over shape anisotropy. Figure taken from [20].

In our studied systems and choice of coordinates, the z-axis becomes a magnetic easy axis and the IP axes become hard axes. In section 2.2.1 the energy cost of spin orientation along the easy or hard plane is worked out for the entire system.

2.1.2 Material

For the ferromagnetic layer Cobalt (Co) is often used. The method of creating the samples is by sputtering which is further described in section 6.1.1. For this method the use of Cobalt as the ferromagnetic layer is convenient, since its materialistic properties are such that it attaches well to the antiferromagnetic underlayer due to epitaxial matching of the lattice structures.

The nonmagnetic layers are mostly formed with Platinum (Pt), and sometimes other heavy metals with the $5d$ electron shell occupied. Platinum atoms have a high spin-orbit coupling which turns out to be an essential ingredient for the DMI. The Platinum also exhibits a strong hybridization with the Cobalt, resulting in a large PMA.

In some experiments Iridium (Ir) is used to form a layer on top of the ferromagnetic layer. It turns out that the Iridium layer reverses the sign of the DMI for the sample [21], however it is not yet understood why this effect occurs. In section 3.3 the effect of this extra layer will be discussed and a possible explanation is given.

The metallic layers are grown on a substrate, consisting of 500μ m Silicon Si, with approximately 100nm silicon dioxide (SiO_2) on top. The theoretical work of this Thesis applies to a broader range of structures and different types of metals, although the above mentioned materials are the ones used in the experimental work of this Thesis. In figure 6 a typical sample is illustrated schematically.

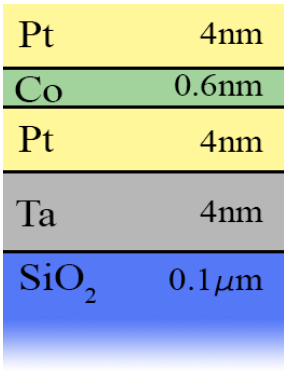

Figure 6: Typical sample $Ta(4)\backslash Pt(4)\backslash Co(0.6)\backslash Pt(4)$

2.2 Domain Walls

Because of the PMA, the spins in the ferromagnetic layer are either pointing up or down. At nonzero temperature it is possible have multiple domains in the ferromagnetic layer with a different orientation perpendicular to the plane of the layers. Between two such domains there is a domain wall where the orientation of the spins rotates continuously between the different domain orientations over a finite length, the DW width, from here on denoted as λ.

From literature we know and in this Thesis we also demonstrate that how the spin orientation flips in a DW is crucial information for driving the DW and can be determined by the properties of the sample, such as the anisotropy or the DMI, and external factors, such as a magnetic field [4, 5, 6, 7, 22]. Let us denote the magnetization direction in the ferromagnetic layer by a unit vector,

$$\vec{\Omega} = \begin{pmatrix} \cos(\phi)\sin(\theta) \\ \sin(\phi)\sin(\theta) \\ \cos(\theta) \end{pmatrix}, \tag{2}$$

where ϕ is the azimuthal angle, and θ the polar angle.

To describe whether a DW goes from an up domain to a down domain, or the other way around, as the x-coordinate increases we define the domain wall charge Q of the DW,

$$Q = \begin{cases} +1, \text{ if } \lim_{x\to\pm\infty}\Omega_z = \mp 1 \\ -1, \text{ if } \lim_{x\to\pm\infty}\Omega_z = \pm 1 \end{cases}. \tag{3}$$

So at a DW the polar angle θ rotates from 0 to π if $Q = 1$ or from π to 0 if $Q = -1$. In section 2.2.2 the profile of θ is calculated for a simple system. It

is the azimuthal angle ϕ that determines properties relevant for the driving of a DW.

In literature a distinction is often made between two types of DWs. The Néel wall has it's magnetic orientation always in the x-z plane (where the x-axis is now chosen to be perpendicular to the DW), so either $\phi = 0$ or $\phi = \pi$ corresponding to a clockwise or counterclockwise sense of rotation respectively. For the Bloch wall the azimuthal angle is either $\phi = \frac{\pi}{2}$ or $\phi = \frac{3\pi}{2}$, meaning that if the x-coordinate increased the magnetization start pointing out of the x-z plane to flip its orientation. In figure 7 the two different types are illustrated. Note that these two types of DWs are extremes; the value of ϕ can (and often will) lie somewhere in between these purely Bloch or Néel states.

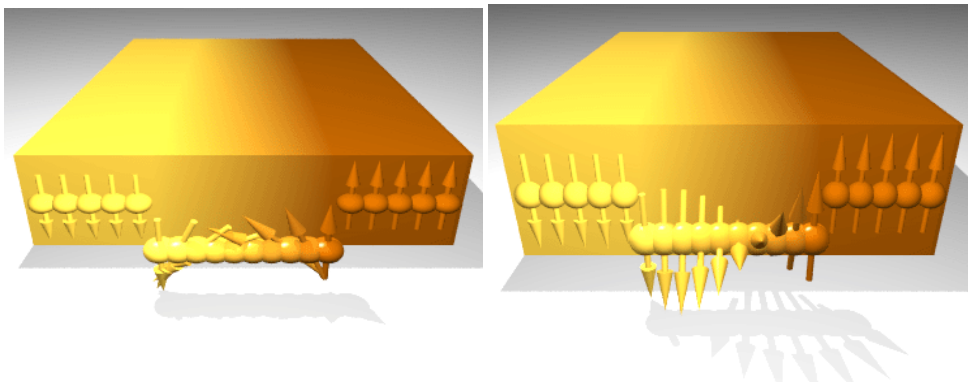

(a) The Néel wall

(b) The Bloch wall

Figure 7: Two types of DWs. Figure adapted from [23]

2.2.1 Energy Density

To study a DW a convenient starting point is the energy of the system. In the most simple case there are three effects at play that contribute to the energy density. Namely, the exchange interaction, the anisotropy and the external magnetic field.

The exchange interaction actually gives rise to ferromagnetism and originates from the Pauli exclusion principle and Coulomb repulsion between two neighboring spins. It is energetically favorable for the two spins to align. A misalignment of neighbors gives an energy contribution proportional to $\vec{\Omega}(\vec{x}) \cdot \vec{\Omega}(\vec{x} + \vec{a})$, where $\vec{a}$ the vector connecting two neighbors. To find the total energy one needs to sum over all particles and their neighbors. In the continuum limit the sum becomes an integral over space and the difference in magnetization for a spin with its neighbors becomes a spatial derivative. Given the spin exchange energy J_s and the lattice spacing a we find the

exchange energy to be

$$E_{exchange}[\vec{\Omega}] = \int \frac{d\vec{x}}{a^3} \frac{J_s}{2} (\nabla \vec{\Omega}(\vec{x}))^2. \tag{4}$$

where J_s is the spin exchange stiffness with dimensions Jm^2. Here, $\nabla\vec{\Omega}$ is to be interpreted as the ∇ operator working on the components of $\vec{\Omega}$. The factor $\frac{1}{2}$ compensates for the doublecounting of neighbors. By partial integration we obtain the more commonly found expression

$$E_{exchange}[\vec{\Omega}] = \int \frac{d\vec{x}}{a^3} \left(-\frac{J_s}{2} (\vec{\Omega}(\vec{x}) \cdot \nabla^2 \vec{\Omega}(\vec{x})) \right). \tag{5}$$

As mentioned in section 2.1.1 there is an energy cost or gain when a spin aligns itself along a hard or easy axis respectively. To lowest order in $\vec{\Omega}$ this is described by $\pm\frac{K_i}{2}\Omega_i(\vec{x})^2$ where $i = x, y, z$ and $K_i > 0$ is the anisotropy energy constant with dimension J. The factor $\frac{1}{2}$ is mainly a convention by the choice of K_i. If i is an easy axis the energy term becomes negative$(-)$ and positive$(+)$ when i is a hard axis. Again, by taking the summation over all particles we find in the continuum limit

$$E_{anisotropy}[\vec{\Omega}] = \int \frac{d\vec{x}}{a^3} \left(\frac{K_x}{2}\Omega_x(\vec{x})^2 + \frac{K_y}{2}\Omega_y(\vec{x})^2 - \frac{K_z}{2}\Omega_z(\vec{x})^2 \right) \tag{6}$$

The energy contribution of the external magnetic field $\vec{B}$ is the Zeeman energy, given by

$$E_{external}[\vec{\Omega}] = \int \frac{d\vec{x}}{a^3} (-\mu_B \vec{\Omega}(\vec{x}) \cdot \vec{B}), \tag{7}$$

where $\mu_B = 9.27400915(23) \cdot 10^{-24}\mathrm{JT}^{-1}$ is the Bohr magneton.

Assuming for simplicity no external magnetic field, from these three contributions we find the energy density in terms of θ and ϕ by filling in the definition given in equation 2 of the magnetization in terms of spherical coordinates

$$\begin{aligned} \mathcal{E}[\theta, \nabla\theta, \phi, \nabla\phi] = \frac{J_s}{2}((\nabla\theta)^2 + \sin^2(\theta)(\nabla\phi)^2) \\ + \frac{K_x}{2}\cos^2(\phi)\sin^2(\theta) + \frac{K_y}{2}\sin^2(\phi)\sin^2(\theta) - \frac{K_z}{2}\cos^2(\theta), \end{aligned} \tag{8}$$

such that

$$E[\theta, \phi] = \int d\vec{x}\, \mathcal{E}[\theta, \nabla\theta, \phi, \nabla\phi]. \tag{9}$$

2.2.2 Shape

From the requirement that systems in equilibrium obey the Euler-Lagrange equations we use the derived energy density in equation 8 to find equations for the fields $\theta(\vec{x},t)$ and $\phi(\vec{x},t)$. For simplicity we consider the 1D system as in figure 4a with only two domains and one DW. We assume ϕ to be constant and for wires we have that $K_x \ll K_y$ from shape anisotropy. Thus ϕ equals 0 or π, *i.e.* the DW is of the Néel type. The Euler-Lagrange equations then give

$$\frac{\partial \mathcal{E}}{\partial \theta} = \nabla \frac{\partial \mathcal{E}}{\partial(\nabla\theta)}; \tag{10}$$

$$\Rightarrow -\frac{K_z}{2}\frac{\partial \cos^2(\theta)}{\partial \theta} = J_s \nabla^2 \theta. \tag{11}$$

For this system, derivatives with respect to the y and z coordinate can be neglected, so $\nabla\theta = \frac{\partial\theta}{\partial x}$. Now if we multiply equation 11 with $\frac{\partial\theta}{\partial x}$ and integrate over x, we find:

$$-\frac{K_z}{J_s}\cos^2(\theta) + C = (\frac{\partial\theta}{\partial x})^2, \tag{12}$$

with C and integration constant. As we send $x \to -\infty$ we know that $\frac{d\theta}{dx} \to 0$ and $\cos(\theta(x)) \to Q$. So we find $C = \frac{K_z}{J_s}$. Using the goniometric identity $\sin^2 a + \cos^2 a = 1$ and taking the square root we find:

$$Q\frac{\partial\theta}{\partial x} = \sqrt{\frac{K_z}{J_s}}\sin(\theta). \tag{13}$$

Now we can separate variables. A primitive of the function $\frac{1}{\sin(\theta)}$ is $\ln(\tan(\frac{\theta}{2}))$. To find the integration constant we define the DW position r_{DW} as such that $\theta(x = r_{DW}) = \pi/2$. And so we find:

$$\ln\left(\tan(\theta/2)\right) = \frac{Q}{\lambda}(x - r_{DW}), \tag{14}$$

with $\lambda = \sqrt{\frac{K_z}{J_s}}$ a typical length scale for the DW width. Here we can clearly see how properties of the material influence the DW width λ, *i.e.* the exchange interaction tries to keep λ small, whilst the anisotropy favors larger values of λ. The above equation we can rewrite to:

$$\theta(x) = 2\arctan(e^{\frac{Q}{\lambda}(x - r_{DW})}), \tag{15}$$

We now have an expression for the form of the magnetization in a static situation. To account for arbitrary azimuthal angles ϕ and study the time dependence we make the DW position and the azimuthal angle dependent on time. So we get te system:

$$\theta(x,t) = 2\arctan(e^{\frac{Q}{\lambda}(x - r_{DW}(t))}); \tag{16}$$

$$\phi(x,t) = \phi_0(t). \tag{17}$$

Throughout this Thesis we make the ansatz that θ and ϕ will remain of this form when the DW is moving.

2.3 Dzyaloshinskii-Moriya-Interaction

A fourth important contribution to the energy of the system comes from the DMI which was proposed around 1959 by Dzyaloshinskii and Moriya [24, 25]. The DMI is a main theme in this Thesis because its theory is still in development. In 1980 Fert suggested that several experimental results can be explained by the DMI as an effect between two spin particles and a spin-orbit coupling atom in a system with Structural Inversion Asymmetry (SIA) [26]. Understanding the origin and effects of the DMI is still a popular topic of research [8, 27].

Suppose we have two spin particles $\vec{S}_A$ and $\vec{S}_B$ close to a surface of a bulk material with high spin-orbit coupling. Now there is a closest atom in the bulk material. Denote the vectors from this atom to the spin particles as $\vec{r}_A$ and $\vec{r}_B$. The situation is illustrated in figure 8. The DMI strength is proportional to these vectors [26],

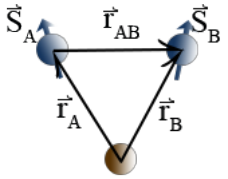

Figure 8: Model of two spin particles(S_A and S_B) interacting with a high spin-orbit atom via the DMI.

$$E_{DMI} \propto \frac{\hat{r}_A \cdot \hat{r}_B}{|\vec{r}_A||\vec{r}_B||\vec{r}_{AB}|}(\hat{r}_A \times \hat{r}_B) \cdot (\hat{S}_A \times \hat{S}_B). \quad (18)$$

This characterization of the DMI we use in this Thesis. Note that depending on the mechanism of describing magnetism, other characterizations are possible, for example in terms of Berry phase theory [27].

2.3.1 Estimate of Magnitude

Experimental research shows that for Spin-Hall-Torque (SHT) driven DW's there can be an offset in the DW speed with respect to the external longitudinal magnetic field [3, 4, 7, 12]. The DMI is used to explain this phenomenon, because in the equations of motion the DMI term, like the external longitudinal magnetic field term, appears in front of the cosine as will be discussed in section 2.3.2.

However, this explanation is only valid if the DMI strength is of the same order as the other terms in the equations of motion. The strength of the DMI is estimated according to this offset in the magnetic field. But by using the following relation for the atomic model we can calculate the real DMI strength [26], using

$$E_{DMI} = -V_1 \frac{\sin(k_F(|\vec{r}_A| + |\vec{r}_B| + |\vec{r}_{AB}|) + \frac{\pi}{10}Z_d)(\hat{r}_A \cdot \hat{r}_B)}{|\vec{r}_A||\vec{r}_B||\vec{r}_{AB}|}(\hat{r}_A \times \hat{r}_B) \cdot (\hat{S}_A \times \hat{S}_B), \quad (19)$$

with

$$V_1 = -\frac{135\pi}{32}\frac{\lambda_d J_s^2}{E_F^2 k_F^3}\sin(\frac{\pi}{10}Z_d). \tag{20}$$

Here, the vectors are displayed in figure 8. We consider a Platinum atom for the high spin-orbit coupling atom for this material is often used in experiments. In equation 20, λ_d is the spin-orbit coupling constant for a d-electron. For platinum we have $\lambda_d \approx 0.5eV \approx 8 \times 10^{-20}$J. Furthermore, J_s is the exchange interaction energy term. A typical value is $J_s \approx 4 \times 10^{-21}$J. The term E_F is the Fermi energy; $E_F = \frac{\hbar^2}{2m_e}k_F^2 \approx 9.3 \times 10^{-20}$J for platinum. The Fermi wavenumber is k_F; $k_F = \sqrt[3]{3\pi^2 n}$ with n the number of free electrons per unit volume. For platinum we have $k_F \approx 3.9 \times 10^9 \mathrm{m}^{-1}$. Finally, Z_d is the number of electrons in the d-subshell. For platinum there are five.

We also approximate the length of the vectors $|\vec{r}_A| \approx |\vec{r}_B| \approx |\vec{r}_{AB}| \approx 5 \times 10^{-10}$m and that the angle φ between $\vec{r_A}$ and $\vec{r_B}$ equals $\varphi = \frac{\pi}{3}$rad. We fill in these values, in equations 20 and 19 to find:

$$V_1 \approx 6 \times 10^{-51} m^3 J, \tag{21}$$

So now we state that the energy contribution is

$$E_{DMI} = \vec{A}_{DMI} \cdot (\hat{S}_A \times \hat{S}_B), \tag{22}$$

where $|\vec{A}_{DMI}| = |A_{DMI}\hat{y}| = A_{DMI} \approx 10^{-23}J$. Later on we will compare this value with experiments where a DMI strength is found by fitting to the data. To do this, we first determine how this DMI strength A_{DMI} we found enters the energy density.

2.3.2 Contribution to Energy Density

To extend this result on the atomic scale to a length scale over the entire material we transform $\hat{S}_A$ to a more general spin at position x, namely $\vec{\Omega}(x)$ the magnetization unitvector. Then we approximate the spin of the neighboring spin particle ($\hat{S}_B$) in terms of $\vec{\Omega}(x)$: $\hat{S}_B \approx \vec{\Omega}(x) + a\frac{\partial\vec{\Omega}(x)}{\partial x}$, where $a \approx 5 \times 10^{-10}$m is the distance between two particles. We now have

$$\begin{aligned} E_{DMI} &= A_{DMI}\sum_i \left(\hat{y} \cdot (\vec{\Omega}(x_i) \times \vec{\Omega}(x_{i+1}))\right) \\ &= A_{DMI}\sum_i \left(\hat{y} \cdot (\vec{\Omega}(x_i) \times (\vec{\Omega}(x_i) + a\frac{\partial\vec{\Omega}}{\partial x}|_{x=x_i}))\right) \\ &= A_{DMI}a\sum_i \left(\hat{y} \cdot (\vec{\Omega}(x_i) \times (\frac{\partial\vec{\Omega}}{\partial x}|_{x=x_i}))\right). \end{aligned} \tag{23}$$

Once again, we take the continuum limit, transforming the summation over lattice positions to an integral over $\frac{dx}{a}$. We then obtain the DMI energy:

$$E_{DMI} = A_{DMI}\int \frac{dx}{a}(\hat{y} \cdot (\vec{\Omega}(x) \times \frac{\partial\vec{\Omega}}{\partial x}). \tag{24}$$

For neighboring particles along the y direction we find a similar expression via the same method. So the total DMI energy contribution becomes

$$E_{DMI} = A_{DMI} \int \frac{d\vec{x}}{a^3} (\hat{y} \cdot (\vec{\Omega} \times \frac{\partial \vec{\Omega}}{\partial x} - \hat{x} \cdot (\vec{\Omega} \times \frac{\partial \vec{\Omega}}{\partial y}). \tag{25}$$

There is no contribution in the z direction, because the interface is in the x-y plane, so from integrating over the z coordinate, we only obtain a factor of order a.

The order of magnitude of the A_{DMI} term is approximated as $|A_{DMI}| \approx 10^{-23}$J. When experimental data is fitted to a model with DMI [4], one finds that de DMI constant is of the order $10^{-24} \sim 10^{-23/-24}$J, which is of the same order as our found value for A_{DMI}. This shows that the DMI effect of the form as suggested by Fert [26] could be of relevance in studying the motion of a DW.

Equation 25 already is of the from of an integral of an energy density over space. For completeness we denote here the total energy density in terms of the spherical coordinates θ and ϕ.

$$\begin{aligned} \mathcal{E} = &\frac{J_s}{2}(\nabla\theta)^2 + \frac{K_x}{2}\cos^2(\phi)\sin^2(\theta) + \frac{K_y}{2}\sin^2(\phi)\sin^2(\theta) \\ &- \frac{K_z}{2}\cos^2(\theta) + A_{DMI}\left(\cos(\phi)\frac{\partial\theta}{\partial x} + \sin(\phi)\frac{\partial\theta}{\partial y}\right). \end{aligned} \tag{26}$$

We will use this energy density throughout this Thesis.

2.3.3 Long Range Effect

To estimate the effect of atoms in the second layer of the high spin-orbit coupling material we will express the effect ϵ_2 of one atom in the second layer in terms of the effect ϵ_1 of the above atom in the first layer. The ratio $\eta = \frac{\epsilon_2}{\epsilon_1}$ will tell us the relevance of atoms in the second layer. The model studied is illustrated in figure 9.

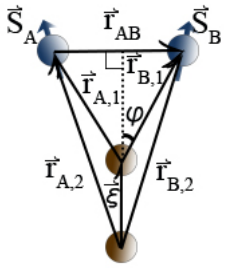

Figure 9: Model of two spin particles interacting with high spin-orbit atoms via the DMI.

We express the vectors $\vec{r}_{A,2}$ and $\vec{r}_{B,2}$ in terms of $\vec{\xi}$, $\vec{r}_{A,1}$ and $\vec{r}_{B,1}$

$$\vec{r}_{A,2} = \vec{r}_{A,1} + \vec{\xi}; \tag{27}$$

$$\vec{r}_{B,2} = \vec{r}_{B,1} + \vec{\xi}. \tag{28}$$

Note that the difference vector $\vec{r}_{AB}$ is the same for the vectors from the atoms. We now make some assumptions to simplify the model and make a well-founded estimate:

- There is symmetry in the y,z-plane, so the x-component of $\vec{r}_{A,1}$ is equal to minus the x-component of $\vec{r}_{B,1}$. Also this gives ξ equals λ times the z-component of $\vec{r}_{A,1}$ or $\vec{r}_{B,1}$.

- The four particles all lie in the x,z-plane, so the y-components of ξ, $\vec{r}_{A,1}$ and $\vec{r}_{B,1}$ are zero and thus $\vec{r}_{B,1,x} = -\vec{r}_{A,1,x} = \vec{r}_{B,1,z}\tan(\varphi)$

Using equation 18, some goniometrics and the linearity of the dot- and crossproduct we find an expression for η in terms of λ and φ

$$\eta = \frac{(1+\lambda)\sec^6(\varphi)(-(1+\lambda)^2+\tan^2(\varphi)}{(\tan^2(\varphi)-1)((1+\lambda)^2+\tan^2(\varphi))^3} \tag{29}$$

In figure 10 the dependence of η on λ and φ is shown. Atoms in the second layer contribute significantly to the DMI because for $\lambda \approx 1$ and $\frac{\pi}{16} \leq \eta \leq \frac{\pi}{5}$ we find $\eta \approx 0.25$. This implies that effects of the lower layers contribute significantly to the DMI energy. As we can see from equation 29 the energy is inversely related to the distance squared.

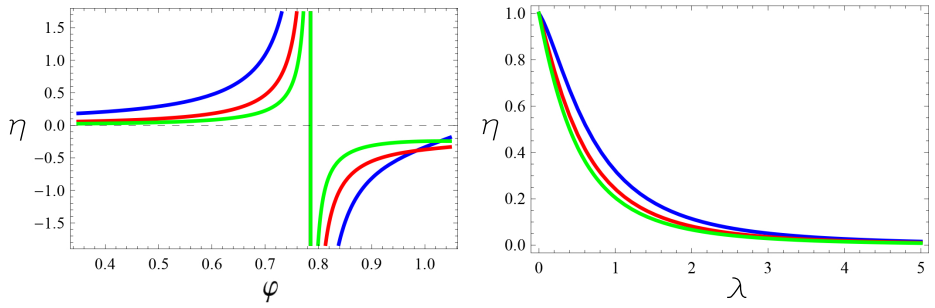

(a) (b)

Figure 10: Graphs of the ratio $\eta = \frac{\epsilon_2}{\epsilon_1}$. **a:** η is plotted as a function of φ for $\lambda = 1$ (Blue), $\lambda = 2$ (Red) and $\lambda = 3$ (Green). **b:** η is plotted as a function of λ for $\varphi = \pi/6$ (Blue), $\varphi = \pi/7$ (Red) and $\varphi = \pi/8$ (Green).

2.4 Domain-Wall Motion

Now that we have an expression for the energy density and the fields $\theta(x,t)$ and $\phi_0(t)$ we can study the dynamics of the system. Ultimately, we are interested in finding an equation for the DW velocity, denoted by $\dot{r}_{DW}$. Here, we work out three ways to obtain equations of motion for the DW. The first method makes use of the Landau-Lifschitz-Gilbert (LLG) equation directly, which describes the time evolution of the magnetization function. In the second method the equations of motion are obtained by varying the corresponding action of the system. This method is in fact equivalent to working out the LLG equation. The third is quite a different approach and

uses the phenomenological theory of creep to calculate the DW speed, as suggested by Lemerle [10].

By combining the previous subsections we obtain an expression for the energy density which includes the DMI

$$\begin{aligned}\mathcal{E}[\Omega, \nabla\Omega] = &\frac{J_s}{2}(\nabla\vec{\Omega}(\vec{x}))^2 \\ &+ \left(\frac{K_x}{2}\Omega_x(\vec{x})^2 + \frac{K_y}{2}\Omega_y(\vec{x})^2 - \frac{K_z}{2}\Omega_z(\vec{x})^2\right) \\ &- g\vec{\Omega}\cdot\vec{B} + A_{DMI}(\hat{y}\cdot(\vec{\Omega}\times\frac{\partial\vec{\Omega}}{\partial x} + \hat{x}\cdot(\vec{\Omega}\times\frac{\partial\vec{\Omega}}{\partial y}),\end{aligned} \tag{30}$$

or, in terms of θ and ϕ we obtain equation 26. We shall use these specific energy densities to determine the equations of motion.

2.4.1 Landau-Lifschitz-Gilbert Equation

The time evolution of the magnetization is successfully described by the LLG equation [28]. The equation is given by

$$\frac{\partial\vec{\Omega}}{\partial t} + \vec{v}_s\cdot\nabla\vec{\Omega} = \vec{\Omega}\times\vec{H}_{eff} - \alpha_G\vec{\Omega}\times\left(\frac{\partial\vec{\Omega}}{\partial t} + \frac{\beta}{\alpha_G}\vec{v}_s\cdot\nabla\vec{\Omega}\right), \tag{31}$$

where v_s is the injected spin current proportional to the current density, α_G is the Gilbert damping constant, β is a dimensionless parameter accounting for the dissipative spin-transfer-torque (STT) and $\vec{H}_{eff} = -\delta E/\hbar\delta\vec{\Omega}$ is the effective field determined by the functional derivative of the energy E of the system. From the energy density given by equation 30 we can calculate $\vec{H}_{eff}$. It is given by

$$\begin{aligned}-\hbar\vec{H}_{eff} = \frac{\delta E[\vec{\Omega}]}{\delta\vec{\Omega}} = &-J_s\vec{\nabla}^2\vec{\Omega} + K_x\vec{\Omega_x} + K_y\vec{\Omega_y} - K_z\vec{\Omega_z} - g\vec{H} \\ &+ 2A_{DMI}(\hat{x}\times\partial_y\vec{\Omega} - \hat{y}\times\partial_x\vec{\Omega})\end{aligned} \tag{32}$$

We assume that the DW is straight and perpendicular to the long axis of the wire, so we study a system as in figure 4a. Next, we insert the functional derivative back in the LLG equation 31 and project the result on the variables r_{DW} and ϕ_0 using equations 16 and 17, and taking the inner product with $\partial\vec{\Omega}/\partial r_{DW}$ and $\partial\vec{\Omega}/\partial\phi_0$ respectively. By integrating over the spatial coordinates we then obtain a system of two coupled differential

equations for r_{DW} and ϕ_0, given by

$$\begin{aligned}\frac{\hbar}{\lambda}(1+\alpha_G^2)\frac{\partial r_{DW}}{\partial t} &= \frac{v_s}{\lambda}\hbar(1+\alpha_G\beta) + Qg\alpha_G B_z + \frac{Q}{2}(K_x-K_y)\sin(2\phi_0) \\ &\quad + Q\frac{\pi}{2}gB_y\cos(\phi_0) + \frac{\pi}{2}(\frac{A_{DMI}}{\lambda} - QgB_x)\sin(\phi_0);\end{aligned} \tag{33}$$

$$\begin{aligned}\hbar(1+\alpha_G^2)\frac{\partial \phi_0}{\partial t} &= Q\frac{v_s}{\lambda}\hbar(\alpha_G-\beta) - gB_z + \frac{\alpha_G}{2}(K_x-K_y)\sin(2\phi_0) \\ &\quad + \frac{\pi}{2}\alpha_G gB_y\cos(\phi_0) + \frac{\pi}{2}\alpha_G(Q\frac{A_{DMI}}{\lambda} - gB_x)\sin(\phi_0).\end{aligned} \tag{34}$$

From 33 we see the velocity is determined by the OOP magnetic field B_z and the applied current v_s, as expected, but also by the IP fields and the DMI. In this light, the DMI can be accounted for as an effective IP field $H_{DMI} = A_{DMI}/g\lambda$ at the position of the DW always pointing perpendicular to the DW, *i.e.* in the x-direction. The time evolution of ϕ_0 is described by equation 34 which, unfortunately, cannot be solved analytically. However, this equation does give insight in the behavior of the DW; because we expect azimuthal magnetization angle ϕ_0 to stabilize in physical systems, $\partial\phi_0/\partial t$ will be equal to zero and therefore we see that in systems with a high DMI the DW will be of the Néel type, whilst a large anisotropy constant K_x favors the Bloch DW type.

Now, by considering only an external OOP magnetic field or only a spin current we can see how the DW is driven by these forces. In the case where also $A_{DMI} = 0$ there is an analytical solution, given by

$$\frac{dx}{d\tau} = Q\frac{B_z}{B_c} + \frac{v_s\beta}{v_c\alpha_G} + \frac{1}{1+\alpha_G^2}\sqrt{(\frac{B_z}{B_c} + \frac{v_s}{v_c}\frac{\beta-\alpha_G}{\alpha_G})^2 - 1}, \tag{35}$$

where we defined the rescaled time $\tau = \frac{(K_x-K_y)t}{2\hbar}$ and DW position $x = \frac{r_{DW}}{\lambda}$, the critical magnetic field $B_c = \frac{\alpha_G(K_x-K_y)}{2g}$ and current $v_c = \frac{\lambda(K_x-K_y)}{2\hbar}$. The physical solution is given by the real part of the solution. The results are plotted in figure 11. An important feature we see in the plots is the so called Walker-Breakdown point; beyond a certain strength of the driving force, the velocity drops when the force is increased. This occurs due to the fact that the azimuthal DW angle ϕ_0 cannot stabilize as follows from equation 34, meaning that ϕ_0 starts precessing, resulting in an oscillatory motion and a less efficient driving of the DW.

When we introduce the DMI in the equations of motion, the system no longer has an analytical solution. The numerical results are plotted in figure 12. The plots clearly show an effect of the DMI on the Walker-Breakdown point. With the method of numerical solving we can also account for IP magnetic fields. Later on in this Thesis we will study the dynamics of the system in more detail using this numerical method.

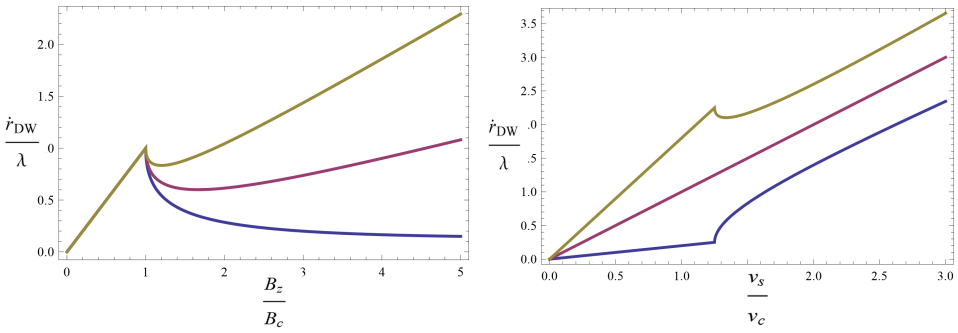

(a) (b)

Figure 11: Plots of the DW velocity as a function of the scaled magnetic field and current showing the Walker-Breakdown phenomena. (a) OOP magnetic field dependence of DW velocity for $\alpha_G = 0.1$ (blue), $\alpha_G = 0.5$ (purple) and $\alpha_G = 0.9$ (brown). (b) Spin current dependence of DW velocity for $\alpha_G = 0.5$ and $\beta = 0.1$ (blue), $\beta = 0.5$ (purple) and $\beta = 0.9$ (brown).

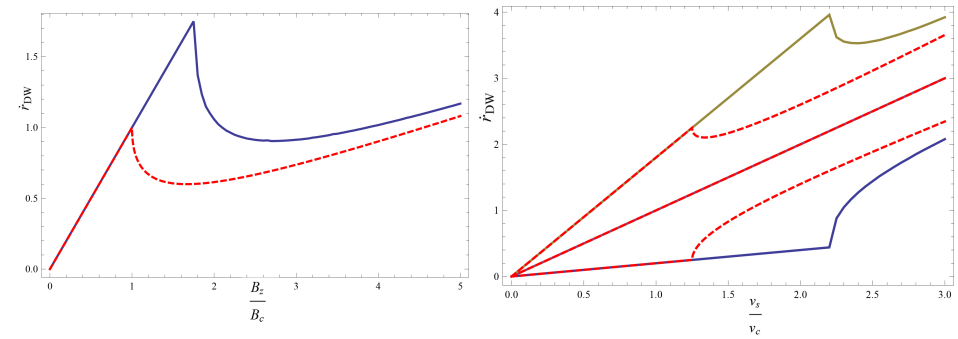

(a) (b)

Figure 12: Plots of the DW velocity with $A_{DMI} = A_c = \lambda(K_x - K_y)/\pi$. The red dashed lines correspond to the solutions with $A_{DMI} = 0$ as in figure 11. (a) OOP magnetic field dependence of DW velocity for $\alpha_G = 0.5$. (b) Spin current dependence of DW velocity for $\alpha_G = 0.5$ and $\beta = 0.1$ (blue), $\beta = 0.5$ (purple) and $\beta = 0.9$ (brown).

2.4.2 Variation of the Action

A well known method of deriving equations of motion is by use of the Hamilton Formalism. It states that the action is minimized in a system in equilibrium. From this principle the Euler-Lagrange equations are derived which have also been used in a simpler form in section 2.2.2. We can obtain an effective action from the energy of equations 8 and 9. If we fill in the assumption for θ and ϕ from equations 16 and 17, and integrate over space, again for a system as in figure 4a, we find an action in terms of r_{dw} and ϕ_0.

We leave out constant constant terms, to find the following action [28]

$$\begin{aligned} A(r_{dw},\phi_0) = \int dt \frac{\lambda}{a^3}\Bigg(-\hbar(\frac{r_{DW}}{\lambda}\dot{\phi_0} + \frac{v_s}{\lambda}\phi_0) - \frac{K_x}{2}\cos^2(\phi_0) \\ - \frac{K_y}{2}\sin^2(\phi_0) + gQB_z\frac{r_{dw}}{\lambda} \\ + \frac{\pi}{2}(QgB_x - \frac{A_{DMI}}{\lambda})\cos(\phi_0) + Q\frac{\pi}{2}gB_y\sin(\phi_0)\Bigg). \end{aligned} \tag{36}$$

We can obtain equations of motion by varying this action. However, dissipation is not included in these equations. To account for damping, we introduce the dissipation functional:

$$\begin{aligned} R(\Omega) &= \hbar\alpha_G \int dt \int \frac{dx}{a^3}\left((\frac{\partial}{\partial t} + \frac{\beta}{\alpha_G}\vec{v_s}\cdot\nabla)\Omega\right)^2 \\ &= \frac{\hbar\alpha_G}{a^3}\int dt\left(\frac{1}{\lambda^2}(\frac{\beta}{\alpha_G}v_s - \dot{r_{dw}})^2 + \dot{\phi_0}^2\right). \end{aligned} \tag{37}$$

The equations of motion are found by solving

$$\frac{\delta A(\Omega)}{\delta\Omega} = \frac{\delta R(\Omega)}{\delta\dot{\Omega}}, \tag{38}$$

which gives

$$\frac{\delta A(\Omega)}{\delta r_{dw}} = \frac{\delta R(\Omega)}{\delta \dot{r_{dw}}}; \tag{39}$$

$$\frac{\delta A(\Omega)}{\delta \phi_0} = \frac{\delta R(\Omega)}{\delta \dot{\phi_0}}, \tag{40}$$

by use of which we find

$$\dot{\phi_0} + \alpha_G\frac{\dot{r_{dw}}}{\lambda} = \frac{\beta v_s}{\lambda} + \frac{QgB_z}{\hbar}; \tag{41}$$

$$\begin{aligned} \frac{\dot{r_{dw}}}{\lambda} - \alpha_G\dot{\phi_0} = \frac{v_s}{\lambda} + Q\frac{K_x - K_y}{2\hbar}\sin(2\phi) \\ + \frac{\pi}{2\hbar}\left((\frac{A_{DMI}}{\lambda} - QgB_x)\sin(\phi_0) + QgB_y\cos(\phi_0)\right). \end{aligned} \tag{42}$$

This is a system of two equations which is equivalent to equations 33 and 34.

2.4.3 Creep Theory

To study the motion of domains in systems with disorder and at a finite temperature the theory of creep can be used. The creep theory is valid for DW driving forces $f \ll f_c$, the so-called creep-regime, where f_c is the

critical driving force at which the DW starts moving at $T = 0K$. When $f \gg f_c$, the so-called flow-regime, the DWs move as if there is no disorder and the velocity depends linearly on f. When f approaches f_c the DW motion enters the depinning-regime, where the dependence on f of the DW velocity changes continuously from exponential to linear. The regimes are illustrated in figure 13. It is interesting to point out that creep theory applies to a broader range of systems than just the motion of magnetic domains. Also the expansion of a water droplet on paper or cracks in a solid medium are well described by this theory [10, 29].

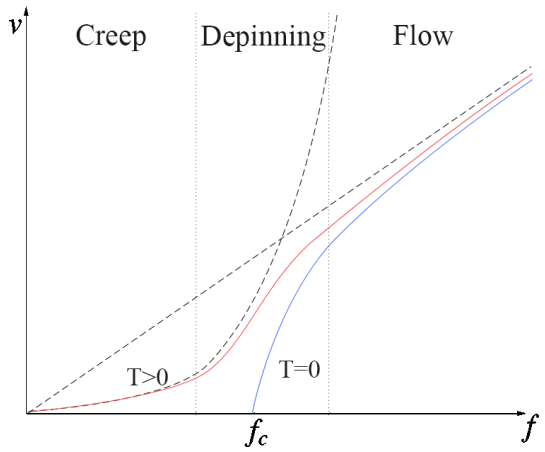

Figure 13: Driving force f dependence of the DW velocity in the creep-, depinning- and flow-regime. The dashed lines indicate exponential and linear behavior. The dotted lines arre the boundaries of the regimes. Figure adapted from [29].

The theory of creep is mostly useful for studying motion under an applied external magnetic field as a driving force [10]. Expansions of magnetic domains in 2D, as in figure 4c will be studied in this Thesis with the use of the theory of creep.

As mentioned in the introduction, in the creep regime the velocity of the DW depends via an exponential relation on the driving force described by equation 1. This follows from the well known Arrhenius law as we will show here. The theory of creep is based on DW motion through some potential energy landscape by thermal fluctuations. The argument of the exponential function is given by the the minimized free energy change ΔF_{min}, divided by the thermal energy $k_B T$. This free energy is minimized over the length L of a DW segment that hops a distance u over the potential

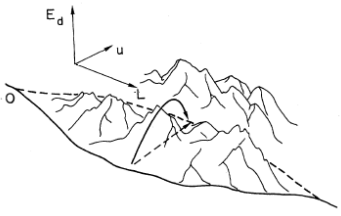

Figure 14: Due to disorder the energy landscape for the DW has hills. By thermal fluctuations the DW can hop over these hills. Figure taken from [30].

landscape by a thermal fluctuation as shown in figure 14.

So, to obtain an expression for the DW motion using creep theory, we need to determine ΔF and minimize it. To determine ΔF we need to ask ourselves the question what changes energetically if a DW segment of length L hops over a distance u. One important effect is that the DW stretches and bends, giving a local increase in DW length. The energy corresponding to this change in length is $\epsilon_{DW}\delta l$ where ϵ_{DW} is the energy per unit length of the DW and δl is the increase in DW length. To calculate the contribution, assume $u \ll L$ and make the second order approximation $\delta l = 2(\sqrt{u^2 + L^2} - L) \approx u^2/L$.

The other effect is that the area of the domain increases which means that more spins align with the applied external magnetic field (that is, when $sign(u) = sign(QB_z)$), lowering the Zeeman energy by a factor $-2H_z\mu_0 M_s t\delta A$ where μ_0 is the magnetic permeability, M_s the saturation magnetization, t the thickness of the ferromagnetic layer and $\delta A = Lu$ the increase in area.

Combining the two contributions, we find the free energy

$$\Delta F = \epsilon_{DW}\frac{u^2}{L} - 2M_s t\mu_0 HLu. \tag{43}$$

Now, u is a function of L, with the proportionality $u \propto u_c(\frac{L}{L_c})^\zeta$ [31]. In this proportionality u_c is the roughness of the DW segment, $L_c = (\epsilon_{DW}^2\xi^2/\Delta V)^{1/3}$, ζ is the wandering exponent and ξ is the correlation length of the disorder potential V with strength ΔV. Using this proportionality, we set the derivative of the above free energy with respect to L to zero, to find the value of L for which the free energy is minimal. To solution is given by

$$L = L_c\left(\frac{\epsilon_{DW}u_c}{2M_s t\mu_0 B_z L_c^2}\frac{2\zeta - 1}{\zeta + 1}\right)^{\frac{1}{2-\zeta}}. \tag{44}$$

Plugging this back in equation 43 we obtain the minimized free energy difference

$$\Delta F_{min} = \epsilon_{DW}^{\frac{1-\mu}{3}}u_c^{2+\mu}\xi^{-\frac{2+4\mu}{3}}\Delta V^{\frac{1+2\mu}{3}}\frac{2\zeta}{1+\zeta}\left(\frac{2\zeta - 1}{2(\zeta + 1)}\right)^\mu (M_s t\mu_0 B_z)^{-\mu}, \tag{45}$$

with $\mu = (2\zeta - 1)/(2 - \zeta)$.

Now the Arrhenius law states that the rate k_{hop} of a hopping event is proportional to the Boltzmann weight of the minimized free energy difference, $k_{hop} \propto \exp(-\Delta F_{min}/k_B T)$. The hopping rate times the hopping distance gives us the DW speed, so also the DW speed is proportional to this exponent. Now, by defining the energy constant $U_c = (\mu u_c/2(\mu + 1)\xi)^\mu\epsilon_{DW}u_c^2/(1+\mu)L_c$ and the critical magnetic field $B_c = \epsilon_{DW}\xi/M_s t L_c^2$ we obtain the final expression for the DW speed:

$$\dot{r}_{DW} = v_0\exp\left(\frac{-U_c}{k_B T}\left(\frac{B_c}{B_z}\right)^\mu\right), \tag{46}$$

with v_0 some proportionality constant. The result corresponds to the literature [31, 32].

Since the theory of creep is well applicable to DWs driven by magnetic fields, this theory will also be used in this Thesis to study the effect of IP magnetic fields and the DMI on the DW motion. It will be studied which terms in this theory are dependent on the IP magnetic field in order to understand experimental results.

3 Fluctuating Dzyaloshinskii-Moriya-Interaction

Most models of DW motion which include the DMI assume that the effect of the DMI is constant throughout the material. However, the DMI is caused by an interaction between spins and atoms with a large spin-orbit coupling [26] as explained in section 2.3, so the DMI certainly fluctuates at an atomic length scale. Furthermore, in experimental research no perfect epitaxial interfaces between the ferromagnetic and nonferromagnetic layer can be created, which may cause the DMI to fluctuate on an even larger length scale. As is shown in figure 15 the interfaces are not even well defined.

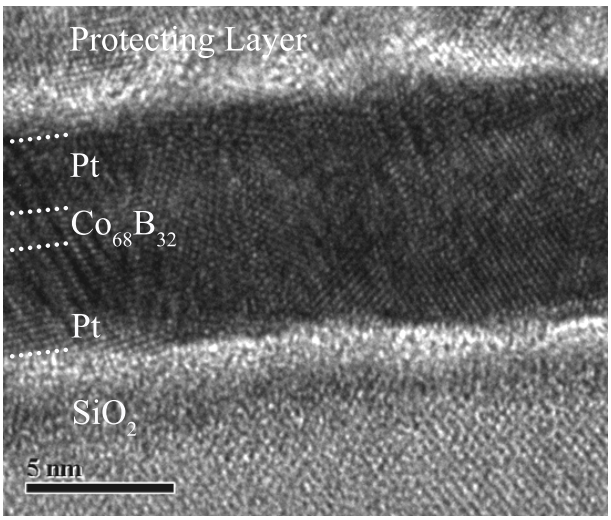

Figure 15: This high resolution transmission electron microscopy image of a $Pt(4nm)\backslash Co_{68}B_{32}(0.6nm)\backslash Pt(6nm)$ trilayer, formed by sputter deposition, shows that the interface between layers is far from perfect.

If the lengthscale of these DMI fluctuations becomes of the same order as the DW width λ there might be an effect of these fluctuations in the equations of motion. In this section it is studied what the effects are of these fluctuations on different length scales and if these effect are relevant in the study of DW motion. First, we will estimate the order of magnitude of the DMI fluctuations by studying different interface profiles. Next, we determine the equations of motion with a variable DMI using the method described in section 2.4.2. These equations will give insight in how the DMI fluctuations affect the DW motion. We will then calculate the DMI energy for different interface profiles to determine the averaged effective DMI for the system. This analysis will be used as a possible explanation for certain experiments.

3.1 Estimate of Magnitude

To estimate the effect on the DMI strength of imperfections in the PMA material, we study three models of what the interface might look like on an atomic scale. These models are illustrated in figure 17. For these three models the total energy due to DMI will be calculated involving only nearest neighbors of the heavy atoms with strong spin-orbit coupling.

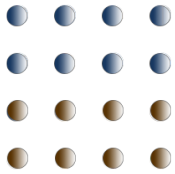

Figure 16: Perfect model of the interface between two layers

We know the effect of second layer interactions from the calculations in section 2.3.3, so this approximation will be rough and an extension to including more interactions than just those of the nearest neighbors might be necessary. The energy of each model will be compared to the energy of a perfect interface as in figure 16.

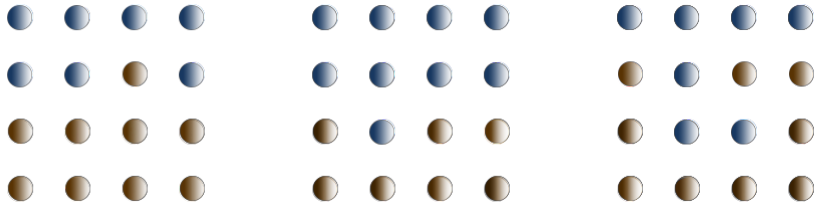

Model 1 Model 2 Model 3

Figure 17: More realistic models of the interface between two layers of the PMA material. These models will be studied in order to estimate the size of fluctuations in the DMI.

For simplicity we first assume that the magnetization direction changes by an equal amount when we move an atomic distance along the x-direction, that is $\partial_x \vec{\Omega}$ is constant. This gives that the crossproduct between two horizontally neighboring spins has a constant value, independent of the position in the model. And the crossproduct between two vertically neighboring spins is zero, because they are pointing in the same direction. In figure 18 the possible configurations of a spin-orbit coupled atom and two spin particles are illustrated with their associated energy.

If we include boundaries, the total energy due to DMI in the perfect model, as in figure 16, equals 8ϵ. Simple counting of the possible configurations and energies gives us the energies in table **??** for the three models as in figure 17.

Model	1	2	3
Energy	2ϵ	2ϵ	3ϵ

Table 1: Energies of the models. **??**

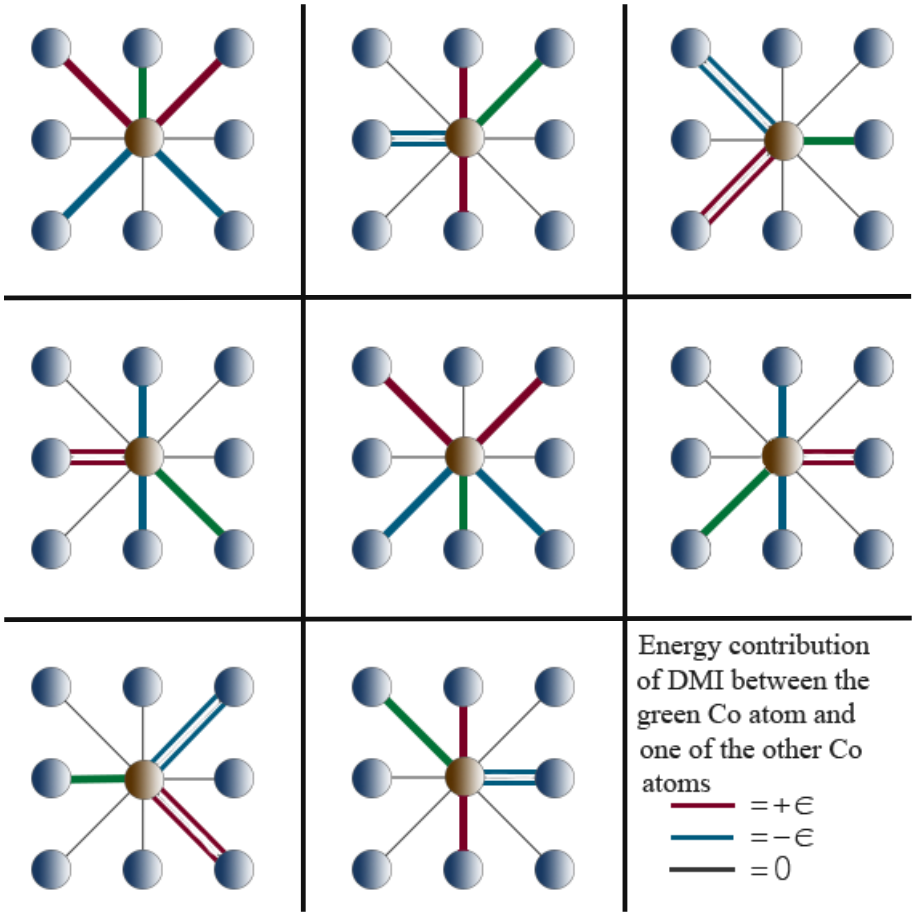

Figure 18: Energy contribution due to the DMI caused by an interaction between de spin particle marked with the green line and one of the neighbors with the central heavy spin-obit coupling atom in the centre.

This tells us that on a length scale of 4 times the distance between atoms, the DMI energy can fluctuate with an amplitude of $63 \sim 75\%$ of the average DMI energy for these models.

The imperfections in the surfaces studied here are still quite modest, the sputtering technique is not as will become more clear in section 6. Intermixing of Pt atoms in the Co layer can certainly occur and the interface roughness can be much higher. As we will show in section 3.3 there can even be certain types of surfaces that give rise a DMI energy of opposite sign. Here we have shown that the DMI can certainly fluctuate on larger lengthscales, so before studying more interfaceprofiles we first study how a nonconstant DMI enters the equations of motion for DWs.

3.2 Effect on Equation of Domain-Wall Motion

Let us redo the variation of the action to obtain equations of motion as in section 2.4.2, but now taking de DMI strength to be a function of position x, so $A_{DMI} = A_{DMI}(x)$. The action remains the same as in equation 36, however, when we now integrate over space we also have to include the position dependence of A_{DMI}. So if we introduce the variable DMI by

$$D_{DMI}(r_{dw}) \equiv \int_{-\infty}^{\infty} A_{DMI}(x) \frac{\partial \theta(x, r_{dw})}{\partial x} dx, \tag{47}$$

we obtain an effective action of the same form as 36 with D_{DMI} instead of $A_{DMI}\pi$:

$$\begin{aligned} A(r_{dw}, \phi_0) = \int dt \frac{\lambda}{a^3} \Bigg(& -\hbar \left(\frac{r_{DW}}{\lambda}\dot{\phi_0} + \frac{v_s}{\lambda}\phi_0\right) - \frac{K_x}{2}\cos^2(\phi_0) \\ & - \frac{K_y}{2}\sin^2(\phi_0) + gQB_z\frac{r_{dw}}{\lambda} \\ & + \frac{\pi}{2}QgB_x\cos(\phi_0) + Q\frac{\pi}{2}gB_y\sin(\phi_0) - \frac{D_{DMI}}{2\lambda}\cos(\phi_0)\Bigg). \end{aligned} \tag{48}$$

Note that if we set $A_{DMI}(x) = A_{DMI,0}$, then, by using the boundary conditions of θ, we get that $D_{DMI} = Q\pi A_{DMI,0}$. Which is in agreement with the calculations for constant DMI as in equation 36.

We now get an extra term when calculating the functional derivative $\frac{\delta A}{\delta r_{DW}}$. Again, by setting the functional derivatives equal to the functional derivatives of the dissipation functional as in equation 37 we obtain the following system of equations:

$$\dot{\phi_0} + \alpha_G\frac{\dot{r_{dw}}}{\lambda} = \frac{\beta v_s}{\lambda} + \frac{QgB_z}{\hbar} - \frac{\lambda}{\hbar}\frac{\partial D_{DMI}}{\partial r_{dw}}\cos(\phi_0); \tag{49}$$

$$\begin{aligned} \frac{\dot{r_{dw}}}{\lambda} - \alpha_G\dot{\phi_0} = \frac{v_s}{\lambda} + Q\frac{K_x - K_y}{2\hbar}\sin(2\phi) \\ + \frac{1}{2\hbar}\left(\left(\frac{D_{DMI}}{\lambda} - Q\pi gB_x\right)\sin(\phi_0) + Q\pi gB_y\cos(\phi_0)\right), \end{aligned} \tag{50}$$

which can be rewritten as

$$\begin{aligned} \frac{\hbar}{\lambda}(1+\alpha_G^2)\frac{\partial r_{DW}}{\partial t} = & \frac{v_s}{\lambda}\hbar(1+\alpha_G\beta) + Qg\alpha_G B_z + \frac{Q}{2}(K_x - K_y)\sin(2\phi_0) \\ & + \left(\frac{\pi}{2}QgB_y + \frac{\alpha_G}{2}\frac{\partial D_{DMI}}{\partial r_{dw}}\right)\cos(\phi_0) + \left(\frac{D_{DMI}}{2\lambda} - Q\frac{\pi}{2}gB_x\right)\sin(\phi_0); \end{aligned} \tag{51}$$

$$\begin{aligned} \hbar(1+\alpha_G^2)\frac{\partial \phi_0}{\partial t} = & Q\frac{v_s}{\lambda}\hbar(\alpha_G - \beta) - gB_z + \frac{\alpha_G}{2}(K_x - K_y)\sin(2\phi_0) \\ & + \left(\frac{\pi}{2}\alpha_G gB_y - Q\frac{1}{2}\frac{\partial D_{DMI}}{\partial r_{dw}}\right)\cos(\phi_0) + \frac{\pi}{2}\alpha_G\left(Q\frac{D_{DMI}}{\lambda} - gB_x\right)\sin(\phi_0). \end{aligned} \tag{52}$$

These equations of motion have many similarities with the equation of motion for constant DMI. The difference is an additional term proportional to $\frac{\partial D_{DMI}}{\partial r_{dw}}$ in the prefactor of the $\cos(\phi_0)$ term. The effect of fluctuations in the DMI acts as an effective magnetic field in the $\hat{y}$-direction at the position of the DW. We see from these equations that for DMI fluctuations the derivative $\frac{\partial D_{DMI}}{\partial r_{dw}}$ has to be of the order $D_{DMI}/\lambda \approx 10^{-15} Jm^{-3}$ to be of relevance for the equations of motion. Fluctuations of this magnitude on the lengthscale of λ can be achieved with certain interface profiles.

3.3 Interface Effects

If we assume that the Co and Pt atoms are arranged on a square lattice, we can systematically study the effect of intermixing, defects and interface roughness on the DMI. For this analysis we will again use the table of energies as in figure 18. The complete set of all possible configurations can be worked out by use of this table. Here, we only mention the interesting and relevant results.

3.3.1 Intermixed atoms

Depending on the softness of the metal underlayer and the velocity of the deposited atoms, atoms of one layer can become embedded the underlying material thus creating an intermixture. In this Thesis we refine our study to systems more or less similar to the stack illustrated in figure 6. So the only relevant type of intermixing that occurs is between the Co layer and the Pt layer. In figure 19 the two different types are illustrated.

Figure 19: The two different possible intermixes. The blue spheres represent Co atoms and the brown spheres represent Pt atoms. (a) An intermixed Pt atom in the Co layer. (b) An intermixed Co atom in the Pt layer.

By assuming periodic boundary conditions we can calculate the two energies of these models in terms of ϵ with the use of figure 18. The calculation of the intermixed Pt atom follows from summing all energy contributions in the energy table and dividing by two. However, one can also use symmetry arguments to obtain the same answer, namely, that the total energy contribution is zero. For the intermixed Co atom there has to be another

Co atom outside the region illustrated in figure 19b in order to have DMI. However, when on top or directly below there is a row of Co atoms the total contribution of the intermixed atom remains zero.

From these simplistic calculations it follows that intermixing has no effect on the DMI. However, as will be discussed in section 6, intermixing should not be ignored because for intermixed Pt atoms, the Co atoms can induce a magnetic moment on the Pt atom, increasing the total magnetic moment of the material.

3.3.2 Defects

In any real lattice, defects can occur, also on the interface between two layers of different material. When such a defect occurs there is a local effect on the DMI. In figure 20 the two relevant kind of defects are illustrated. For comparison the energy of the perfect interface here is 6ϵ. We can easily

(a) (b)

Figure 20: The two different possible defects at the interface. (a) A Pt defect. (b) A Co defect.

calculate the DMI of the models. The results are shown in table 2. Evidently, the absence of a Co atom in the lattice has the greatest effect effect, causing a drop in DMI energy for the below Pt atom and its nearest neighbors, whilst the absence of a Pt atom only reduces the DMI energy for one column.

Model	a	b
Energy	4ϵ	2ϵ

Table 2: Energies of the models of figure 20.

3.3.3 Interface Roughness

Most relevant for fluctuations in the DMI is the interface roughness, as we will see here. There is an infinite number of possible interface structures so we have restricted ourselves to some interesting cases for 4×4 lattice models. By use of the table in figure 18 the DMI energy can be calculated for any given strucure. The models we study are depicted in figure 21.

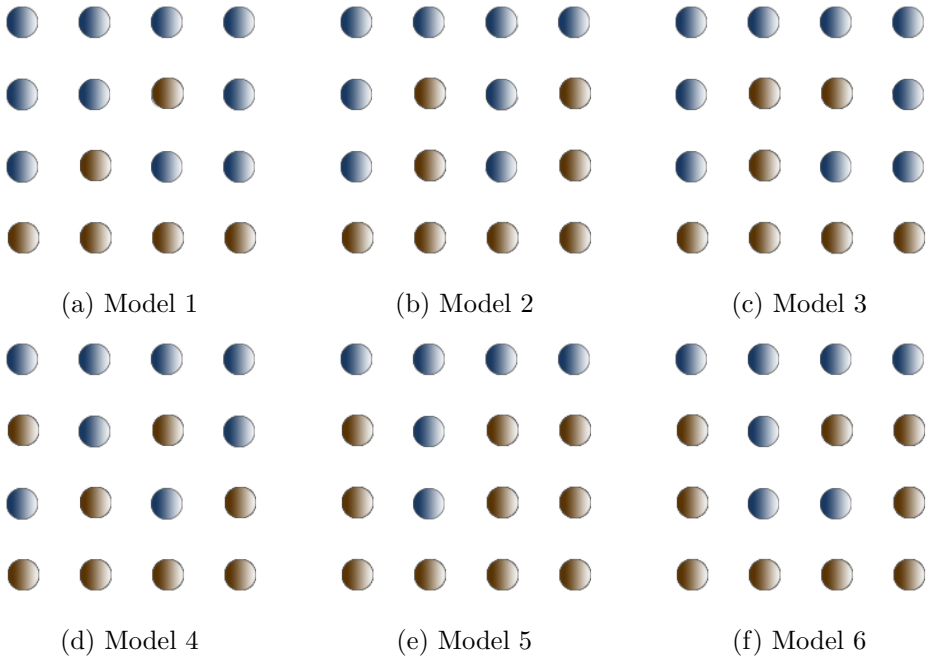

(a) Model 1 (b) Model 2 (c) Model 3

(d) Model 4 (e) Model 5 (f) Model 6

Figure 21: Some of the possible interface structures.

If we again assume periodic boundary conditions, the total DMI energy follows from straightforward calculations. For the perfect interface we have a total energy of 8ϵ as mentioned earlier. In table 3 the energy for the models in figure 21 are given.

Model	1	2	3	4	5	6
Energy	3ϵ	-8ϵ	3ϵ	0	2ϵ	0

Table 3: Energies of the models of figure 21.

The first observation of these results is that the energies never exceed nor reach the 8ϵ value of the perfect interface. So in the roughness some energy is lost by averaging. However, the amount of roughness does not seem to further lower the energy because for example models 1 and 3 have the same energy. A second observation is that in some interface structures the DMI energy contribution is zero. The energy contribution can locally still be nonzero, but averaged over the lattice, the contributions cancel out. The third observation is that for model 2 we find a negative energy contribution which would also result in a negative sign in front of the DMI term in the eqautions of motion.

Especially this third observation is interesting, because recently an article has been published about this very phenomenon, *i.e.* DMI inversion [21]. This sample is quite similar to the one illustrated in figure 6, the only

difference is that there is an extra layer of Iridium (Ir) between the Co layer and the top Pt layer.

A possible explanation for this phenomenon is that due to the materialistic properties of the Iridium, the system prefers to form an interface as model 2, depicted in figure 21b. One possible way to test this hypothesis is to measure the total magnetic moment of the sample and compare this with the expected magnetic moment based solely on the volume of the ferromagnetic material. If the interface is as in model 2, there might be an additional magnetic moment induced on some of the nonferromagnetic atoms.

3.3.4 Hexagonal Lattice

The above study of interface roughness assumes that the atoms of the studied material are ordered in a square lattice. A similar analysis can also be done for the hexagonal lattice. The DMI energy contribution table for the hexagonal lattice is shown in figure 22. We remark that the energy quanta ϵ is not equal for the tables of the square and hexagonal lattice. The effects

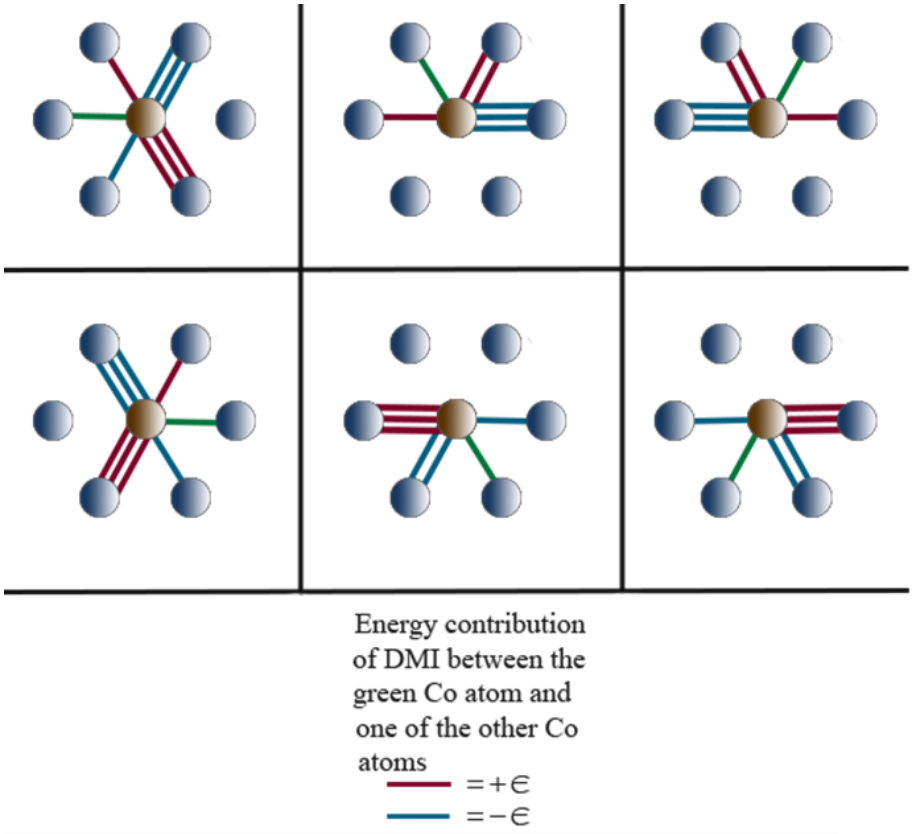

Figure 22: Energy contribution due to the DMI caused by an interaction between de spin particle marked with the green line and one of the neighbors with the central heavy spin-obit coupling atom in the centre.

of defects and intermixing are similar for both lattices due to the same symmetries. Although relevant, in this Thesis the hexagonal lattice will not be further investigated. The study of interface roughness for different lattice types in relation to the DMI could provide valuable input for micromagnetic simulations of DW motion. These simulations can then be used to quantitatively describe the interface roughness by comparing the simulated DMI with experiments.

4 Field Driven Creep Theory

In numerous studies the creep theory as described in section 2.4.3 has been checked and confirmed for simplified cases, *i.e.* one- or two-dimensional PMA systems with only an OOP magnetic field as the driving force. However, here we show that just by introducing an in-plane (IP) magnetic field, the creep theory becomes more complex because, depending on the DW azimuthal angle ϕ, the IP field contributes to the DW energy density and to the driving force $f \propto H_\perp \cos(\phi) + H_\parallel \sin(\phi)$, where $\phi = 0 \quad (\pi/2)$ corresponds to a Bloch (Néel) DW. Also, in PMA multilayers with a structural inversion asymmetry the DMI takes on a crucial role by not only giving an offset in the IP magnetic field component perpendicular to the DW, *i.e.* in the energy density and driving force $H_\perp \rightarrow (H_\perp - H_{DMI})$, but also by affecting the stiffness of the DW as we will show in this section.

4.1 Contributions of the IP Field and DMI

When introducing an IP magnetic field and DMI into the theory of creep, the main question becomes what terms in equations 46 and 45 are in some way dependent on the IP magnetic field or DMI. For this question we propose the answer that the IP magnetic field enters the creep theory in three ways. First, by contributing to the driving force f. Second, by affecting the energy density of the DW and thereby also the azimuthal magnetization angle of the DW, which in turn affects the contribution to the driving force. And third, by influencing the DW stiffness, giving rise to a stiffness renormalization depending on the strength of the DMI and the IP field. In this section these three contributions will be further examined in the light of previous, less complete examinations. In our system of study no current will be applied, but only an external magnetic field $\vec{B} = (B_x, B_y, B_z)$. We will also account for an interfacial DMI.

4.1.1 Driving Force

The driving force of a DW is characterized in the equations of motion. Our starting point here are the equations 33 and 34. For our studied system there is no spin current v_s. Also, suppose for simplicity that $B_y = 0$ and that we study a system with no IP anisotropy, so $K_x = K_y$. By looking for a stable solution for $\dot{\phi}_0$, we find $\phi_0 = \arcsin(2gB_z\lambda/\pi\alpha_G(gB_x\lambda + QA))$ from equation 52, which is a real solution if $2|B_z| \leq \pi\alpha_G|H_{DMI}Q - B_x|$. In this case we find that the DW velocity is given by $v_{DW} = \alpha_G g Q B_z/\hbar\lambda$, from inserting ϕ_0 in equation 51 and thus the IP field dependence is eliminated by ϕ_0. If $2|H_z| > \pi\alpha_G|H_{DMI}Q - B_x|$ the angle ϕ_0 cannot stabilize and keeps on rotating, resulting in a less efficiënt driving of the DW. The closer H_x gets to H_{DMI}, the faster ϕ_0 precesses and so the slower the DW is driven.

So to some extent the IP field influences the driving force for values of B_x around H_{DMI}, resulting in a symmetry not around $B_x = 0$, but around $B_x = H_{DMI}$.

By numerically solving the equations of motion we can determine the DW velocity dependence on the applied IP magnetic field. The result is plotted in figure 23. This plot clearly shows the behavior just described,

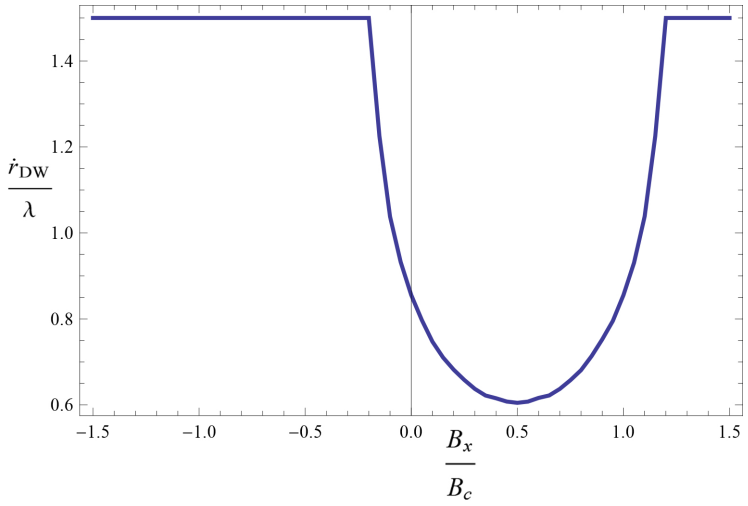

Figure 23: Plot of DW velocity dependence on B_x showing the less efficient driving regime around $H_{DMI} = 0.5B_c$. Here $\alpha_G = 0.5$ and $B_z = 1.5B_c$.

i.e. for large enough B_x the azimuthal DW angle ϕ_0 can stabilize, canceling out the effect of the IP magnetic field and the DMI on the DW motion, but for B_x near H_{DMI} the velocity drops quadratically. The size of this quadratic regime is determined solely by the dimensionless parameter α_G; for small values of α_G the regime becomes bigger. This result thus shows a clear dependence of the driving force on the IP magnetic field and the DMI.

The result is also backed up by experimental research where also this parabola shaped dip is observed around an nonzero value of B_x [21, 31, 32] and also the flattening of the curve is observed for larger values of B_x [33]. Also in the experiments done for this Thesis, these two phenomena have been observed, as we will discuss in more detail in section 6. However, by most experimental research groups, this flattening is not fully understood because they explain the parabolic shape by inserting the IP magnetic field effect in the energy density ϵ_{DW} term in the creep theory which works well for values of B_x around H_{DMI}, but it does not predict the flattening for larger values of B_x. This method will be covered in section 4.1.2.

An important remark to make here is that the method used to calculate these equations of motion and the numerical result of the DW velocity plot do not account for any disorder/pinning potential landscape. Of course, in reality a disorder potential is always present. Therefore, these results

should be interpreted as a characterization of the driving force in the theory of creep, where the disorder potential is considered, rather than a direct result for the DW velocity.

4.1.2 Energy Density

A crucial element of the creep theory is the energy density of the system [10, 30, 31, 32]. As shown in section 2.4.3, the term $U_c(f_c/f)^\mu$ in equation 1 follows from the minimization of the free energy of a DW with length L which moves a small distance $u \ll L$ over the potential landscape. The exponent μ is given by $\mu = (d+2\zeta-2)/(2-\zeta)$, where d is the dimension of the interface and ζ is the wandering exponent. The last term in equation 43 is the energy gain from the increased area which now has a parallel aligned magnetization with the OOP field as illustrated in figure 24 (there is an additional factor of 2 because the image only shows the upper half of the problem). The

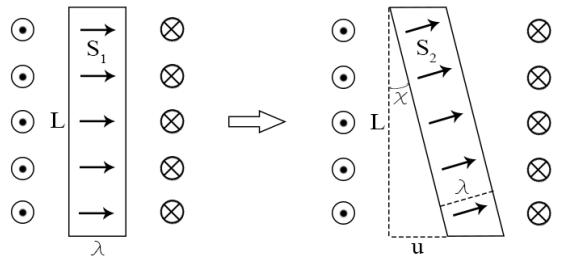

Figure 24: Change of the area of the domains when a Néel DW of length L is displaced by a small distance u. This figure only shows the upper half of the displacement.

same figure also gives insight in how the IP field contributes to the free energy: there is an increase of area with an IP magnetization. So we expect a contribution of $-\pi M_s t \mu_0 (\vec{H}_{DMI} + \vec{H}_{IP}) \cdot \hat{\phi}_0)(2\Delta S)$ where $\hat{\phi}_0$ is direction of the magnetization at the DW ($\hat{\phi}_0 \approx (\cos(\phi_0) - \frac{u}{L}\sin(\phi_0), \sin(\phi_0) + \frac{u}{L}\cos(\phi_0))$) and ΔS is the difference in area between the two boxes in figure 24. We use a small angle approximation $\chi \approx u/L$ so

$$\begin{aligned} 1/\cos(\chi) &\approx \frac{1}{1-\frac{u^2}{2L^2}} \\ &\approx 1 + \frac{u^2}{2L^2}; \end{aligned} \tag{53}$$

$$\begin{aligned}\Delta S &= S_2 - S_1 \\ &= L\frac{\lambda}{\cos(\chi)} - L\lambda \\ &\approx L\lambda(1 + \frac{u^2}{2L^2}) - L\lambda \\ &= \lambda\frac{u^2}{2L}.\end{aligned} \tag{54}$$

So, a contribution of

$$\Delta F_{IP} = -\pi M_s t \mu_0 (\vec{H}_{DMI} + \vec{H}_{IP}) \cdot \hat{\phi_0}) \lambda u^2 / L, \tag{55}$$

from the IP field is expected. This term originates also from the elongation of the DW and can therefore be included in ϵ_{DW}.

Let us study this ϵ_{DW} because it is in the minimized free energy difference of equation 45 to the power $(1-\mu)/3$. For simplicity, assume again that $B_y = 0$. We get a contribution linear in $\frac{u^2}{L}$, independent of the angle ϕ_0. We abbreviate these linear contributions by the stiffness ϵ_{el}. It is called a stiffness, because this term likes to keep the DW segment short and straight. In section 4.1.3 we elaborately investigate this stiffness in relation to the DMI and IP magnetic fields. If we now choose our coordinates as such that the DW segment is parallel to the y-axis, the contribution from the anisotropy is $2K_x\lambda t\cos^2(\phi_0)$. Hence, the energy density is given by

$$\epsilon_{DW} = \epsilon_{el} + 2K_x\lambda t\cos^2(\phi_0) - \pi M_s \lambda t (B_x - H_{DMI})\cos(\phi_0). \tag{56}$$

In this equation ϕ_0 is chosen such that the energy density is minimized. By setting the derivative with respect to ϕ_0 to zero we find that the global minimum is reached for ϕ_0 equal to zero or π when $|B_x - H_{DMI}| \geq \frac{4K_x}{\pi M_s}$ and equal to $\arccos(\pi M_s(B_x - H_{DMI})/4K_x)$ otherwise. If we plug in these results in equation 56 we find that

$$\epsilon_{DW} = \begin{cases} \epsilon_{el} - \frac{\pi^2 \lambda M_s}{4K_x}(B_x - H_{DMI})^2, \text{ when} |B_x - H_{DMI}| \geq \frac{4K_x}{\pi M_s}; \\ \epsilon_{el} + 2K_x\lambda t - M_s\lambda t|B_x - H_{DMI}|, \text{ otherwise.} \end{cases} \tag{57}$$

Now we can insert this energy density in equation 45 to see how the DW velocity depends on the IP magnetic field. For most samples the exponent μ is 1/4, so the power of the IP magnetic field dependence of ϵ_{DW} coincidentally then also is $(1-\mu)/3 = 1/4$. This has led to confusion because in some research groups, the IP magnetic field effect on the energy density in the creep theory is taken to be equivalent to the effect on the driving force from the argument that they both appear in the creep exponent to the same power [21, 31, 32, 21]. However, this is only the case when $\mu = 1/4$.

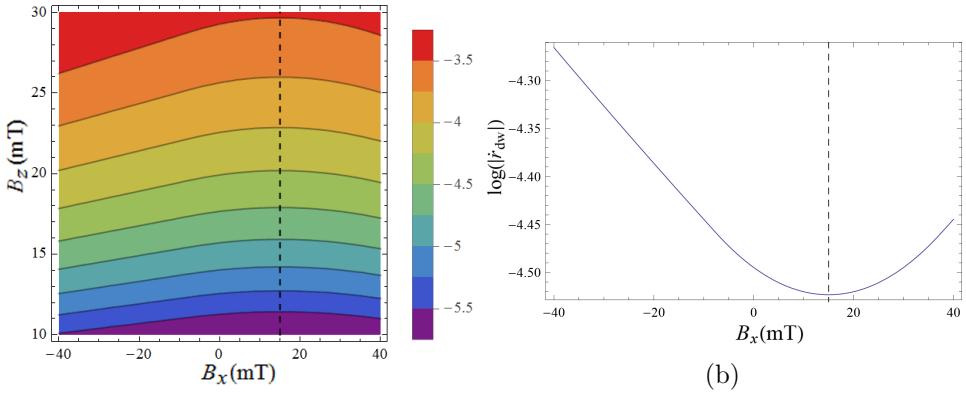

(a) (b)

Figure 25: Plots of the DW velocity dependence on B_x according to IP magnetic field modification of the energy density. Here $H_{DMI} = 15mT$, around this value we observe the symmetry. (a) Contour plot of $\log(\dot{r}_{DW})$ as a function of the IP and OOP magnetic field. (b) Plot of the DW velocity profile against the IP magnetic field B_x.

In figure 25a the result is shown in a contour plot and in figure 25b the velocity is plotted against the IP magnetic field for constant B_z. We see again the symmetry for values of B_x around H_{DMI}.

As mentioned in section 4.1.1 one drawback of this model is that $\dot{r}_{DW} \to \infty$ as $B_x \to \pm\infty$. Intuitively, this is not expected since the azimuthal DW angle will be chosen as such to cancel the strong effect of the IP magnetic field. Also, experimentally a flattening of the velocity is observed [33] and described in section 6.

4.1.3 Effective Stiffness

As we have seen the creep theory is based on a competition between two effects of a displacement u of a DW segment of length L. The energy gain from the increased area of OOP aligned magnetization is balanced by the energy cost of stretching and bending the DW. Here, we further study the cost of bending the DW segment in terms of the stiffness, introduced above as ϵ_{el}.

The exchange stiffness, expressed in the energy density by J_s, immediately characterizes this bending cost because the exchange interaction prefers an alignment of nearest neighbors and therefore a straight DW. However, we show here that the introduction of DMI influences this stiffness. By applying a IP field this DMI contribution can be tuned. To see how this effect arises, we study the system as in figure 4b and consider its energy density. Assume again that there is no IP anisotropy, so $K_x = K_y$. We rewrite the energy density of equation 30 in terms of θ and ϕ_0, where ϕ_0 is assumed to

depend on only on y.

$$\begin{aligned}\mathcal{E}(\theta,\phi_0) = \frac{J_s}{2}\left(\sin^2(\theta)(\partial_y\phi_0)^2 + (\vec{\nabla}\theta)^2\right)\\ - \frac{K}{2}\cos^2(\theta) - g\Big(B_z\cos(\theta)\\ + \sin(\theta)(B_x\cos(\phi_0) + B_y\sin(\phi_0))\Big)\\ + A_{DMI}\Big(\sin(\phi_0)\partial_y\theta\\ + \cos(\phi_0)(\cos(\theta)\sin(\theta)\partial_y\phi_0 + \partial_x\theta)\Big).\end{aligned} \tag{58}$$

The total energy is the integral of $\mathcal{E}$ over the wire. By integration along the thickness and length of the wire and by leaving out the constant terms, we find

$$\begin{aligned}E[\phi_0, X] = \int \frac{L_z dy}{a^3}\Bigg(\frac{J_s}{\lambda}\left(\partial_y X\right)^2 - 2gQB_zX\\ + \pi\left(A_{DMI}Q - g\lambda B_x\right)\cos(\phi_0)\\ - \pi\left(AQ\partial_y X + g\lambda B_y\right)\sin(\phi_0)\Bigg).\end{aligned} \tag{59}$$

In equilibrium, the energy E will be minimized with respect to the free parameters ϕ_0 and X. So by setting the functional derivatives zero we can solve exactly for ϕ_0. We find that ϕ_0 has to obey

$$\pi(A_{DMI}Q - g\lambda B_x)\sin(\phi_0) + (A_{DMI}Q\partial_y X + g\lambda B_y)\cos(\phi_0) = 0. \tag{60}$$

The exact solution for ϕ_0 is

$$\phi_0(y,t) = \arctan\left(\frac{g\lambda H_y + AQ\partial_y X}{g\lambda H_x - AQ}\right), \tag{61}$$

illustrating the IP field and the DW tilt (*i.e.* $\partial_y X$) effect on ϕ_0. This term corresponds with theoretical results found in literature on DW tilting [13, 34]. It also shows that when $g\lambda B_x$ approaches A_{DMI}, the IP field counters the DMI resulting in a Bloch wall ($\phi_0 = Q\pi/2$). When we stay away from this limit, ϕ_0 remains small and we can use a second order approximation $\arctan(x) \approx x$ to find:

$$\phi_0(y,t) \approx \frac{g\lambda B_y + A_{DMI}Q\partial_y X}{g\lambda B_x - A_{DMI}Q}. \tag{62}$$

We plug this in back in the energy E from equation 59 and use again the

small angle approximation $\sin(x) \approx x$ and $\cos(x) \approx 1 - x^2/2$ to find

$$\begin{aligned} E[X] = \int \frac{L_z dy}{a^3} \Bigg(& - 2gQB_z X \\ & + \frac{A_{DMI} g\pi Q\lambda^2 B_y}{A_{DMI}Q - g\lambda B_x} \partial_y X \\ & + \left(\frac{J_s}{\lambda} - \frac{A_{DMI}^2 \pi}{2(A_{DMI}Q - g\lambda B_x)} \right) (\partial_y X)^2 \Bigg). \end{aligned} \tag{63}$$

Now we see three terms in the integral, of which the first is the driving term by the OOP field which we already have seen before. The second induces a tilt $\partial_y X$ in the DW as a direct consequence of a nonzero DMI and the IP B_y field [13, 34]. This second term is competing with the third term, which prefers to keep the line $X(y,t)$ straight and vertical (*i.e.* parallel to the y-axis). The third term is therefore interpreted as the effective stiffness of the DW, inversely related to the elasticity. Interestingly, we observe that the DMI introduces an additional term $\Delta\epsilon_{el}$ to this stiffness. Whereas the usual stiffness is expected to be J_s, we now define an effective stiffness $\tilde{\epsilon}_{el}$ as:

$$\tilde{\epsilon}_{el} = J_s - \frac{A_{DMI}^2 \pi\lambda}{2(A_{DMI}Q - g\lambda B_x)}. \tag{64}$$

In figure 26 $\Delta\epsilon_{el}$ is shown as a function of B_x.

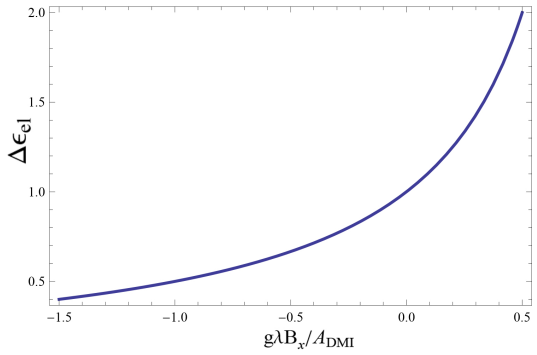

Figure 26: Stiffness contribution $\Delta\epsilon_{el}$ for large DMI

An important feature of this DMI effect on the creep theory is that it is antisymmetric around $B_x = H_{DMI}$. A DW segment becomes more elastic when B_x is more negative, whilst the segment gets a higher stiffness for larger positive B_x. Intuitively, this can be understood in the following way. Suppose the DMI is dominant forcing the DW to be of the Néel type. Consider now a positively charged DW, then if B_x is positive, it aligns with the magnetization at the DW. Now bending the DW would cause the magnetization at the DW to misalign with the IP field, being energetically

less favorable. So in this case, due to the DMI the DW is more stiff. Now suppose B_x is negative and therefore antiparallel with the magnetization at the DW. Any bending of the DW would now be energetically favorable because the antiparallel alignment costs the most energy, thus making the DW more elastic.

To study if the addition of $\Delta\epsilon_{el}$ to the stiffness is significant, we compare the orders of magnitude of J_s and $A_{DMI}\lambda$. To estimate J_s we use that $\lambda = \sqrt{J_s/K_z}$ so $J_s = \lambda^2 K_z$. Experimental measurements suggest a value for K_z in the order of $K_z \approx 10^{4\sim5} Jm^{-3}$ (see section 6), which is also found in literature [4, 32]. In the same literature the typical value $\lambda \approx 10^{-(8\sim9)}m$ is used for the DW width. So J_s is estimated by $J_s \approx 10^{-(11\sim14)} Jm^{-1}$. In section 2.3.1 the value of A_{DMI} is estimated by a calculation on the atomic scale with the result $A_{DMI} \approx 10^{-(3\sim4)} Jm^{-2}$, which is of the same order as found in experiments [4]. And so $A_{DMI}\lambda \approx 10^{-(11\sim14)} Jm^{-1} \approx J_s$. This is quite a rough estimation but it does show that the DMI contribution to the stiffness can be significant. For a better approximation we consider the fitted parameters: $J = 10^{-11} Jm^{-1}$, $K = 2 \cdot 10^5 Jm^{-3}$ and $A = 5 \cdot 10^{-4} Jm^{-2}$ so $\lambda = 7nm$ and $A\lambda = 4 \cdot 10^{-12} Jm^{-1}$ [4]. So in this case the two terms differ only in half an order of magnitude.

Note that this contribution to the stiffness is only valid in the regime where $H_{DMI} \gg B_x$, as mentioned before. When B_x approaches the H_{DMI} value, the azimuthal DW angle ϕ_0 goes to $Q\pi/2$ and the contribution to the stiffness is lost.

4.2 Modified Creep Theory

We have seen that the driving force, the energy density and the stiffness of the DW are influenced by the IP magnetic field and the DMI. The question now is how these three effects are translated to one model describing the motion of the DW.

For these three contributions there are three partly overlapping regimes that are of relevance.

- For the driving force the regime where $2|B_z| > \pi\alpha_G |H_{DMI}Q - B_x|$ is of relevance.
- In the energy density a distinction between the regime $|B_x - H_{DMI}| \geq \frac{4K_x}{\pi M_s}$ and its complement has to be made.
- The effective stiffness correction is only valid when $|B_x - H_{DMI}| \gg 1$.

We cannot explicitly describe how the driving force modification enters the theory of creep because we only have a characterization of it. To include the effective stiffness, we can just insert the result in the energy density computation by adding the term $A_{DMI} Q \partial_y X \sin(\phi_0)$ before minimizing over ϕ_0. The minimization is then no longer solvable by analytic methods, so we

compute the energy density numerically. The results will be shown and extended to 2D models in section 5.

An important remark to make here is that there might be more effects of the DMI and IP magnetic field on the theory of creep. One such effect might be that the DW width λ can depend on the DMI and IP magnetic field, which is intuitively quite reasonable. This DW width λ occurs almost everywhere in the calculations of DW motion, so if there is an effect on λ it is likely to be significant.

5 Models of Domain-Wall Motion

Up to now, we have discussed multiple methods of deriving the equations of motion which take into account the DMI and the IP magnetic field. To test the validity of these methods and their results we need to compare them with experiments. Most experiments consist of observing the expansion of a 1D domain as in figures 4a and 4b, or a 2D domain as in figure 4c. Therefore, to compare theory with experiment we need to develop models of DW motion for these 1D and 2D systems, which is exactly what we will do in this section. This section will mostly be a demonstration of results since the underlying theory and methods have already been covered in the previous sections.

First, we consider the LLG and use the numerical solving method to study how 1D DWs move with a DMI and IP magnetic field. To some extent this has already been done in section 2.4.1. Then we extend this method to 2D system and study the time evolution of a circular domain. Next, we consider how the theory of creep extends to 2D systems, because this theory does take into account the disorder potential. In this approach we will consider the theory of creep that is used by other research groups and found in literature, as well as the theory of creep suggested in section 4.

5.1 Landau-Lifschitz-Gilbert Equation

The equations of motion, 33 and 34, that have been derived from the LLG equation in section 2.4.1 can only be solved analytically in simplified cases, *e.g.* with only a OOP magnetic field B_z and no DMI or IP magnetic field. So to study the DW dynamics for more generalized situations, we solve the obtained equations of motion numerically. Recall the scaling parameters we introduced earlier: $\tau = \frac{(K_x - K_y)t}{2\hbar}$, $x = \frac{r_{DW}}{\lambda}$, $B_c = \frac{\alpha_G(K_x - K_y)}{2g}$, $v_c = \frac{\lambda(K_x - K_y)}{2\hbar}$ and $A_c = \lambda(K_x - K_y)/\pi$.

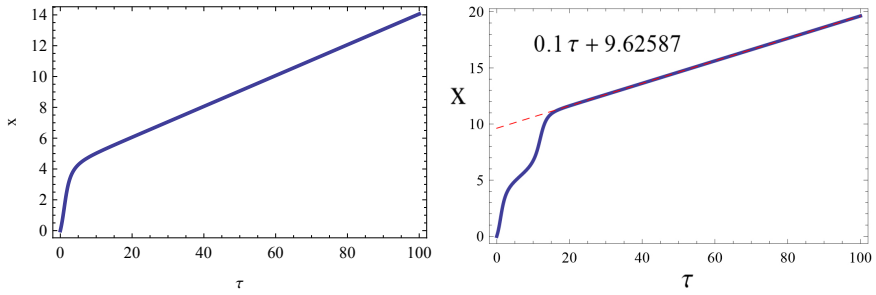

(a) (b)

Figure 27: Results of the numerical solution method. (a) Time evolution of the rescaled DW position. We can see that the motion becomes constant after some time. (b) Linear fit (dashed red line) to the DW position. To be sure that the DW velocity has stabilized, the fit is made to the numerical data after 300 time units.

In figure 27a we see the time evolution of the rescaled DW position. It approaches constant motion after approximately 20 units of time. We determine the average DW velocity by making a linear fit after 300 units of time - to be safe - which is shown in figure 27b. To test if this method works well, we calculate the velocities with the numerical method for the simplified cases and then compare it with analytical result. As we can see in figure 28, the numerical method of determining the velocity works well.

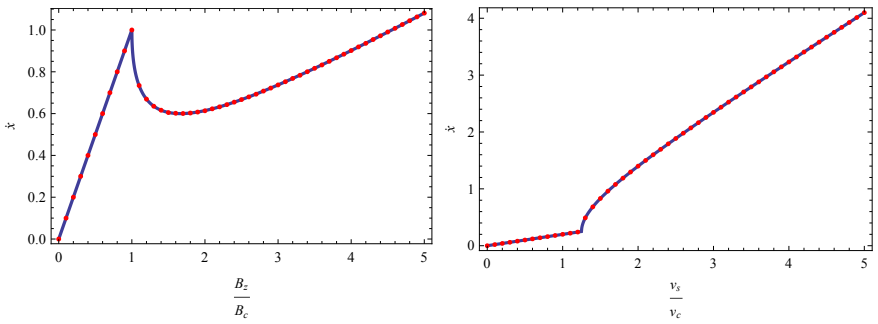

(a) (b)

Figure 28: Comparison of the numerical method (red dots) with the analytical method (blue line). The numerical data agrees well with the analytical result.

Now that we have confirmed the legitimacy of our method, we can study the behavior of the DW velocity with DMI and IP magnetic fields. For the 1D model we have already shown the DW velocity profile with respect to the IP magnetic field along the x direction in figure 23. Here, in figure 29, we show it again along with the DW velocity profile for an IP field along the y direction. The important feature of the profile in figure 29a is the domain

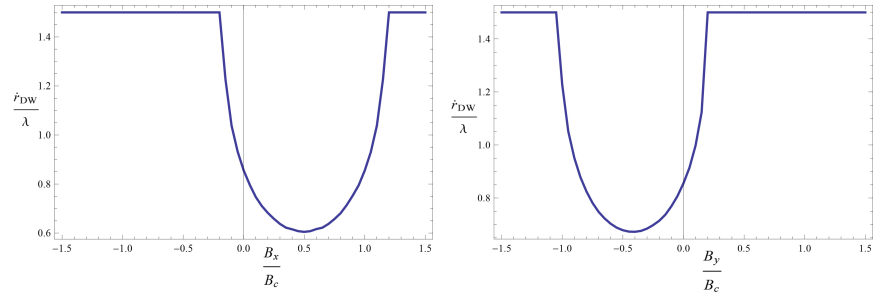

(a) (b)

Figure 29: DW velocity profiles with respect to the IP magnetic fields B_x (a) and B_y (b)

around H_{DMI} where the velocity drops parabolically. It follows directly from the equation of motion 34 for ϕ_0 that the width of this domain is exactly $B_z \frac{4}{\pi \alpha_G}$, as discussed in section 4. So for small values of the dimensionless Gilbert damping parameter α_G, this domain becomes larger. The relevance

of this result has already been discussed in part and will become more clear when our experimental results are described in section 6.

In figure 29b the same phenomenon occurs. This is also due to the same fact that the azimuthal DW angle ϕ_0 cannot stabilize, *i.e.* there is no value of ϕ_0 such that $\dot{\phi}_0$ as in equation 34 equals zero, so the driving of the DW becomes less efficient because energy is lost in the motion of ϕ_0.

For the study of 2D system we extend the 1D models in the following way: In the 2D system we assume a circular up-magnetized domain centered at the origin. We use polar coordinates φ and r_{DW} to describe the shape of the DW. We apply an IP field along the cartesian x direction and calculate the DW velocity as a function of the normal $\hat{n}_{DW}$ to the DW given the values of H_{DMI} and B_z. This normal is given by

$$\hat{n}_{DW} = \frac{\partial \vec{r}_{DW}}{\partial \varphi} \times \hat{z}, \tag{65}$$

where we have defined $\vec{r}_{DW} = r_{DW}\hat{r}$ and $\hat{r} = (\cos(\varphi), \sin(\varphi))$.

Next, we apply the 1D model for a moving DW on a line along this normal. For the 1D model we have that the IP field is now given by $\vec{B}_{IP} = B_x \hat{n}_{DW}$. The OOP magnetic field and the DMI do not change for the 1D model. We calculate the velocity of the DW along this normal. Then we translate this velocity to the radial velocity by multiplying it with $\hat{n}_{DW} \cdot \hat{r}$. Then, we let the system evolve a timestep and redo the entire calculation. This method will also be used for extending the theory of creep to 2D models

Now let us extend the 1D results from the LLG to 2D systems by use of the method described above. The result is shown in figure 30 where the lines represent the postion of the DW at different times. The figure shows an asymmetric expansion due to the IP field and the DMI. It also shows that the shape deforms away from the initial circular shape. This result can only be used to speculate about the true expansion shape, since disorder is not accounted for.

5.2 Creep Theory

The models obtained from the LLG equation are not quite representative for real systems because the disorder potential is not taken into account. For comparison with experiments the creep theory is more appropriate. As elaborately discussed in section 4, there are multiple ways to include the DMI and IP magnetic field into the theory of creep. To determine which way suits experimental observations and results best we work out the model found in literature and our own model as described in section 4.2 and extend it to 2D systems.

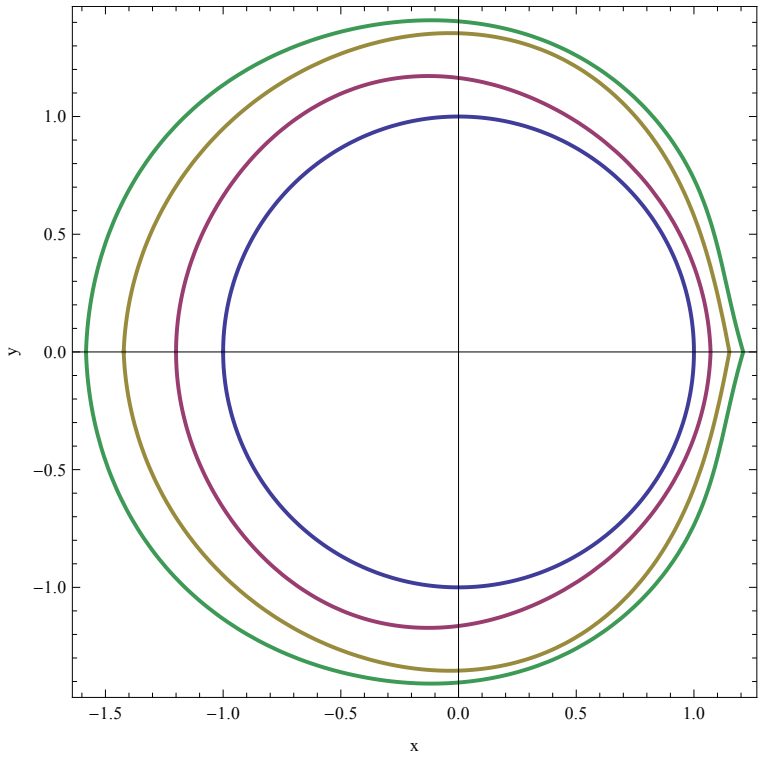

Figure 30: Model of the expansion of a magnetic domain obtained from the LLG equation. The lines indicate the DW position at consecutive time steps.

5.2.1 Regular Creep Theory

In literature, the IP magnetic field is included in the theory of creep only by considering its effect on the energy density [21, 31, 32] as described in section 4.1.2. For 1D systems the resulting velocity profiles have already been shown in figure 25. To extend this result to 2D systems we need to add a term to the energy density for the IP magnetic field, parallel to the length of the DW. In the minimization of the energy density over the azimuthal DW angle we get an additional term $-\pi M_s \lambda t \sin(\phi_0)$.

In figure 31 the result is shown. Here, we also see the asymmetry occurring due to the DMI and IP magnetic field. This shape has been observed in external experiments as well as our own. However, we also observe a much higher degree of deformation, as we will show and discuss in section 6.

5.2.2 Modified Creep Theory

As mentioned in section 4, we have not reached the point where we can give a theory of creep which includes all effects of the DMI and IP magnetic field. We have seen the effect on the driving force, which is emphasized and once again illustrated in section 5.1. In section 5.2.1 we extended the effect of

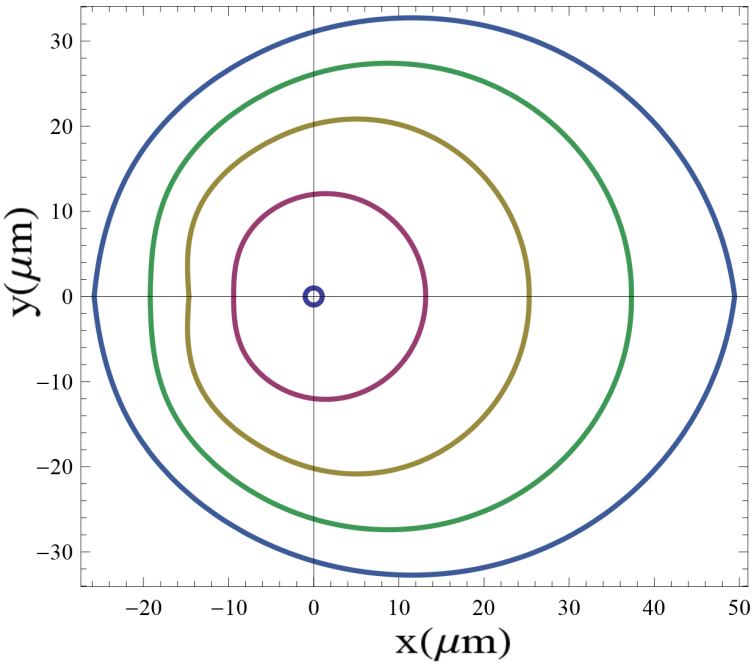

Figure 31: Model of the expansion of a magnetic domain obtained from the theory of creep. The lines indicate the DW position at consecutive time steps

the energy density on the creep theory. Here, we will show the effect of only the stiffness modification.

One of the most important features of this stiffness modification is that it is antisymmetric around $B_x = H_{DMI}$ with respect to the IP magnetic field, whereas the above mentioned and illustrated effects are symmetric around the effective DMI field. This antisymmetry follows from equation 64 which shows that when $H_{DMI} - B_x \to -(H_{DMI} - B_x)$, then $\tilde{\epsilon} - J_s \to -(\tilde{\epsilon} - J_s)$. Recall that this effect is only valid for $|B_x - H_{DMI}| \gg 0$. When B_x approaches H_{DMI}, the arctangens exponentially flattens off to $\pm\pi/2$.

By inserting an exponential flattening for B_x approaching H_{DMI}, we obtain the results for the effect of the stiffness modification on the domain wall motion. The results are illustrated in figure 32.

Extending this result to a 2D domain expansion is beyond the scope of this Thesis as we will use the 1D to gain sufficient insight in the effect of the stiffness modification. Together with the theory described in the previous section we can use this result to suggest an explanation for observations from the experiment of this Thesis, which we shall discuss in the following section.

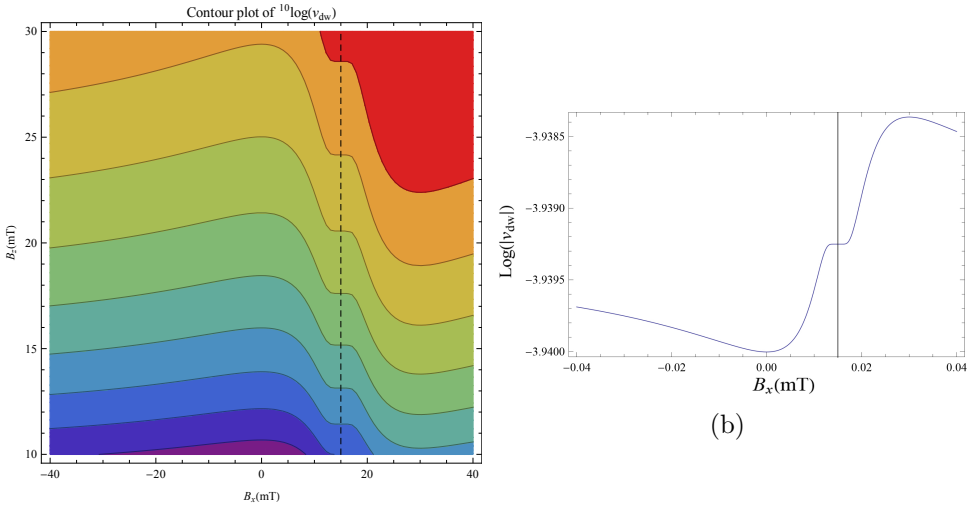

(a) (b)

Figure 32: Plots of the DW velocity dependence on B_x according to IP magnetic field modification of the DW stiffness. Here $H_{DMI} = 15mT$, around this value we observe the antisymmetry. (a) Contour plot of $\log(\dot{r}_{DW})$ as a function of the IP and OOP magnetic field. (b) Plot of the DW velocity profile against the IP magnetic field B_x.

6 Experiment

Fundamental phenomena related to interface effects in layered perpendicular magnetic anisotropy materials are not completely understood. Experimental measurements on PMA materials with SIA give rise to the existence of an interaction between neighboring spin particles near a metal with high spin-orbit coupling, the DMI, as mentioned in 2.3. Motivated by the theoretical work on the fluctuating DMI due to interface structures explained in section 3, we want to study the effect of manipulations to the interface on the DMI. Also, explicit insight in dependence of this DMI on SIA and other interfacial parameters remains to be uncovered.

In this research, we attempt to chart one of these parameters, namely the relative (i.e. top/bottom) interface roughness and intermixing. So we introduce a SIA in a layered material, not by varying the top and bottom layer thickness, nor by varying the type of material, but by creating a difference in the way the interfaces are formed. It is expected that a well-defined, smooth interface gives a different DMI contribution compared with an interface which is more rough and rugged. Recent experimental data show that the behavior of DW motion in PMA materials with SIA varies with changes in the roughness of an interface between the ferromagnetic and nonferromagnetic material [35]. In this research we attempt to study if these changes are correlated to the strength of the DMI by studying the DW velocity profile with respect to the IP magnetic field of the different samples. As mentioned in the previous sections, the effective DMI field H_{DMI} can occur as a symmetry point in these profiles, so the profile can therefore be used as a measurement of the DMI. A key requirement is of course that the profiles are in line with the theory.

We demonstrate in our experiment that there are significant effects on the DW velocity profiles with respect to the IP magnetic field from variations in the interface formation. In terms of the currently known theory for these profiles, our observations cannot be fully understood. This is the main motivation for revisiting the theory of creep in section 4, taking IP magnetic fields and the DMI into account.

In this part of the Thesis, we explain the experiment. Since the theoretical background for this research is already elaborately discussed we start by describing the research method, which ranges from the method of forming samples to data gathering and analysis. Then we give the results of the experiments. In section 7 we interpret these results and compare them with other experiments.

6.1 Method

In order to understand and interpret the obtained data and results from the experiment it is imperative to comprehend the methods of acquisition.

Here, we describe the applications that have been used for our research to form samples and acquire data. First we describe the process of how the samples are formed and how we can change the structure of the interface by varying certain parameters. Next, the Kerr microscopy and experimental setup is explained, which is used to observe the DW and its dynamics. This is followed by the description of the Vibrating Sample Magnetometer (VSM), the Superconducting Quantum Interface Device (SQUID) and the method of High Resolution Transmission Electron Microscopy (HRTEM) which are all used for determining the degree of intermixing and interface roughness of the samples. Finally, we describe the method of determining the strength of the PMA.

6.1.1 Sputter Deposition

In order to study the effects on the DMI strength of SIA by interface roughness and intermixing, we first need to be able to make PMA samples, where we can vary the smoothness of the interface. This can be achieved by control over certain parameters in the process of making the sample. Samples usually are made using the sputter deposition technique, where layers of different material are formed upon each other.

To create a sample by sputter deposition a thin ($\sim 500\mu$m) substrate is placed in an ultra high vaccum chamber of low pressure ($\sim 10^{-6}$Pa) underneath the *target*, which is the material that has to be deposited on the substrate. Next, Argon (Ar) gas is injected into the chamber. Then, a voltage is applied between the target (kathode) and the substrate (anode). This creates a plasma of Ar ions, which are then accelerated towards the kathode due to the electric field. For kinetic energies much bigger that the thermal energies, the collisions between the Ar ions and the target breaks off atoms of the target material, which then are deposited around the chamber and, most importantly, on the substrate. Behind the target a magnet is placed to increase the interaction between Ar-ions and the target. In figure 33 the sputter deposition setup is illustrated schematically.

To form a thin layer of well defined thickness of the target material on the substrate, a mechanical shutter is placed between the target and substrate before turning on the voltage. Then, after turning on the gas flow and the voltage, the shutter is removed and after the right amount of time the voltage is switched off, immediately stopping the sputter deposition.

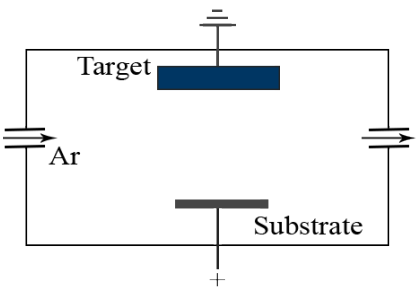

Figure 33: Schematic illustration of the sputter deposition setup.

To determine the right amount of
time, a calibration is needed. This calibration is done by sputtering on the system for a well known long time τ, then by atomic force microscopy the thickness D of the deposited layer is determined to obtain the growthrate $r = D/\tau$. In for our experimental setup we find growthrates of the order of $1\text{Å}\text{s}^{-1}$. In the calibration the error is of order $10^{-3}\text{Å}\text{s}^{-1}$.

For our experiment we study the effect of the Ar gas flow, which determines the pressure inside the sputter chamber at the moment of deposition of the layers of the sample. We expect that by increasing the gas flow the kinetic energy of the broken off atoms is lowered by collisions with the gas, causing the the target atoms to reach the substrate surface with less energy. Therefore the gas flow influences the roughness and intermixing of the interfaces between different deposited materials. So by controlling the gas flow we can influence the interface. For this experiment an array of samples had been made of the structure as in figure 6. However, when depositing the last Pt layer, the Ar gas flow varies for each sample, causing a variation between the samples in the top interface.

The process of making the samples with sputter deposition is sensitive to imperfections and errors since layers are formed of only several atoms thick. Therefore, the samples are cleaned thoroughly to maintain a clean surface. The silicon substrate is used because the surface is perfectly straight on the atomic scale.

6.1.2 Kerr Microscopy

Once the samples are formed we want to determine the DW velocity profiles with respect to the IP magnetic field. So we want to study the motion of DWs. In order to do this we have to be able to observe the magnetic domains. This can be done by the use of the Magneto Optical Kerr Effect (MOKE); when light reflects from a magnetized surface, its polarization can change [36, 37].

For Kerr microscopy the MOKE is used to chart different magnetic domains by the light intensity. A beam of light passes trough a polarization filter and then reflects on the surface of the studied sample. Due to the MOKE, the reflected light pick up a different polarization where also the magnetization of the sample differs. Next, the reflected light passes through the analyzer polarization filter before being captured by a camera. The difference in polarization is then translated to a difference in intensity in the camera image, thereby distinguishing the different magnetic domains. In figure 34 the Kerr Microscopy setup is illustrated schematically.

Due to the PMA in our samples, we only need to distinguish between two types of domains, *i.e.* either up or down. Because we want to observe the regime where DW velocities are of the order of $\sim 10\mu\text{ms}^{-1}$, we use an optical magnification such that the resolution of the obtained image is

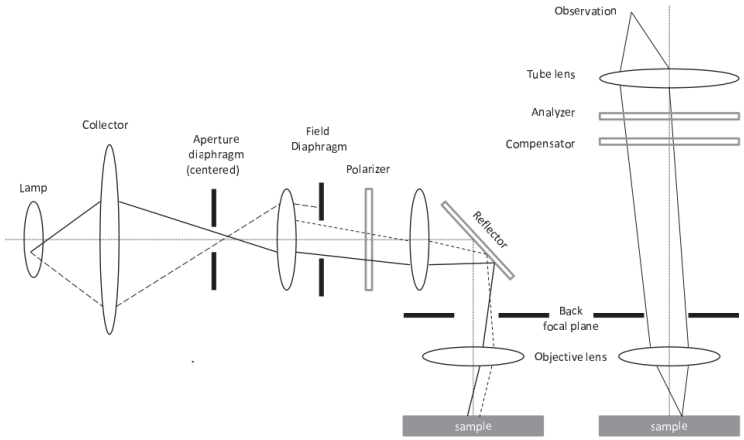

Figure 34: Schematic illustration of the Kerr Microscopy setup. Figure adapted from [40] where more details can be found.

$\sim 30\mu$m per pixel. This length then also becomes the measurement error of the DW position defined here as the boundary between two domains.

To form and expand magnetic domains and study the DW dynamics with an IP magnetic field applied, three electromagnetic coils are used ; one to apply a magnetic field in the z direction, and two with a magnetic core to insure a more homogeneous magnetic field in the x direction. The magnetic field generated by these coils is linear with the applied currents over the coils (as long as the magnetic core is not saturated), so in the experimental setup the magnetic field is controlled by means of controlling the current.

In figure 35 the Kerr microscope with magnetic coils is displayed. By measuring the magnetic field in the center of the setup, the coils are calibrated. For this experiment two sets of coils have been used: The so called 3D magnet (named so because it also has coils for the y direction, but these are not used in this experiment) which can apply an IP magnetic field of up to $\sim$ 40mT (see figure 35a) and an OOP field of maximum magnitude of $\sim$ 100mT (see figures 35b and 35c). The error in the calibrations is $\sim$ 0.05mT for both coils. The second set is the IP magnet with OOP magnet sample holder, which is actually the combination of only two coils generating an IP magnetic field where in the sample holder there is a coil generating an OOP magnetic field, as the name suggests. For the last set, IP magnetic fields of $\sim$ 350mT can be realized, however the OOP magnetic field is limited to $\sim$ 40mT. The error in the calibration for the IP field coils is $\sim$ 0.5mT and for the sample holder coil it is $\sim$ 0.005mT. However, by not perfectly positioning the sample there might be leakage from one field into the other for both sets of coils. This is an experimental feature which is difficult to avoid, so it has to be eliminated in the analysis of the data.

In figure 36 the expansion of a magnetic domain is shown by subtracting

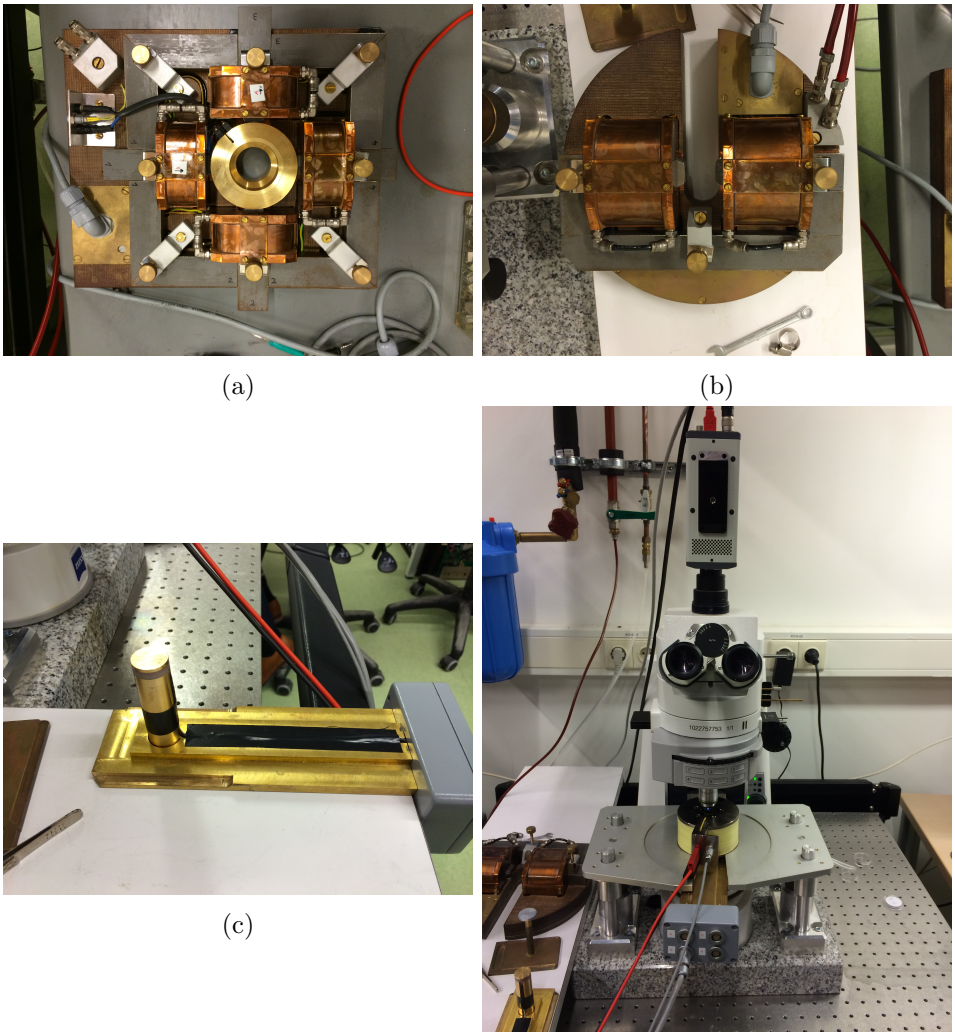

Figure 35: Photo's of the Kerr microscope setup. (a) The 3D magnet. (b) The IP magnet. (c) the OOP magnet embedded in the sample holder. (d) the Kerr microscope.

two images takes at different times. The distance indicated with the arrow, divided by the time difference gives the DW velocity. The data for this experiment are obtained by recording suchs expansions of magnetic domains in a given combination of OOP and IP magnetic field. For each sample we find a suitable OOP field at which the DW moves at velocities of $\sim 10\mu\text{ms}^{-1}$ because this are the speeds that can be accurately measured with lengthy measurement. Then we look for a location in the sample where magnetic domains frequently nucleate. At this position we make recordings of expanding magnetic domains with a fixed OOP magnetic field, but varying the IP magnetic field for each recording over the whole range of possible IP

magnetic fields. This data is then analyzed by determining the DW position as a function of time along a line that has a certain angle with the direction of the applied IP magnetic field. As expected (see sections 2,4 and 5) the DW position scales linear with time, so a linear fit is made to obtain the DW velocity.

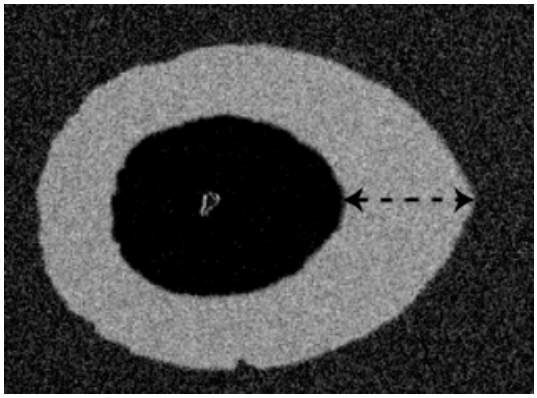

Figure 36: Illustration of the magnetic domain expansion. The figure is obtained by subtracting two images, taken at different times. The velocity can be determined by the distance marked by the arrow, divided by the time difference.

To compensate for the possible leakage of the IP field in the OOP field, another equivalent data set is acquired and analyzed in the same way, but with the OOP field inverted. So we study both positively and negatively charged DWs. By then also inverting the obtained DW velocities, the two velocity profiles should overlap. However, if there is a leakage, the net OOP field would be larger for one dataset, whereas it is smaller for the other, resulting in an increasing difference of measured DW velocities between the two datasets for increasing OOP magnetic fields. The data from figure 41b exhibits this leakage.

To compensate for any leakage the two velocities measured at a fixed OOP field should be somehow averaged, but not in a straight forward way because only for small differences a linear averaging is appropriate. The difference in velocities is caused by a difference in the OOP magnetic fields, so to average correctly between the two velocities, we need to know how the DW velocity scales with the OOP magnetic field. As suggested by the theory of creep, this scaling is exponential $\ln(v_{DW}) \propto B_z^{-\mu}$, so a logarithmical average would be appropriate. To test if indeed the dependence of the DW velocity on B_z is exponential a series of measurements is done where the OOP magnetic field is varied and with no IP magnetic field. This measurement indeed confirms the exponential behavior and also shows that, as expected, $\mu \approx 1/4$. In appendix B the measurement for determining the exponent μ and its results are described.

6.1.3 VSM-SQUID

If the thickness of the ferromagnetic layer, as well as the magnetic moment per unit volume for the ferromagnetic material is known, then by determining the surface area of the sample it can be computed how large the total magnetic moment should be. However, when intermixing between the layers occurs an additional magnetic moment can be induced on the antiferromagnetic particles. So by measuring the total magnetic moment of the sample and subtracting the expected magnetic moment, we can quantize the degree of intermixing between the layers. For the measurement of the magnetic moment the VSM-SQUID apparatus is used, which is the combination of a Vibrating Sample Magnetometer (VSM) and Superconducting QUantum Interference Device (SQUID).

In the SQUID a magnetic flux through a superconducting loop is measured by letting a current enter the loop from one side and exit at the other. From Lenz' law a second current circulates the loop countering the magnetic flux. However, because the flux enclosed by the loop has to be an integer of magnetic flux quanta, the current can also flow in the other direction. A changing magnetic flux thus gives rise to an oscillating current. By placing Josephson junctions in the two branches a voltage arises as a function of the magnetic flux. The VSM measures the magnetic moment of the sample by vibrating a saturated sample inside such a SQUID loop. The vibration causes a change in the magnetic flux passing through the SQUID loop.

This method of measuring the magnetic moment is extremely sensitive and accurate. Typical measured values are $\sim 10^6 \mathrm{Am}^{-1}$ and the measurement error is $\sim 10^4 \mathrm{Am}^{-1}$.

6.1.4 High Resolution Transmission Electron Microscopy

To get an idea of how rough the interface is, one would ideally just take a look at how the atoms are arranged in the sample. This can be done to some extent by the use of High Resolution Transmission Electron Microscopy (HRTEM). The resolution of a HRTEM image is ~ 0.05nm, so rows of single atoms in a crystal can be distinguished. However, in HRTEM images it is difficult to distinguish between different species of atoms. Therefore, this method can only be used to speculate about the roughness of the interface.

To study a sample with HRTEM an ultra thin slab of the sample has to be made, because HRTEM works by transmitting a beam of electrons trough the sample. By use of a Focussed Ion Beam (FIB), such a thin slab can be cut from a sample. During the transmission, electrons interact with the sample, thereby forming an image with some imaging device after passing trough the sample. For our experiment the HRTEM imaging is done by Marcel Verheijen from the Group Plasma & Materials Processing from the Eindhoven University of Technology.

6.1.5 Anisotropy

By using Stoner-Wohlfarth theory, the strength of the PMA can be determined. An external magnetic field B is applied under a certain angle α with the normal to the surface of the sample. Then we measure the component of the magnetization along the easy axis by using the anomalous Hall effect. From this we can determine the angle θ between the easy axis and the magnetization, see also figure 37. The Stoner-Wohlfarth theory then dictates that the total energy of the system, given by

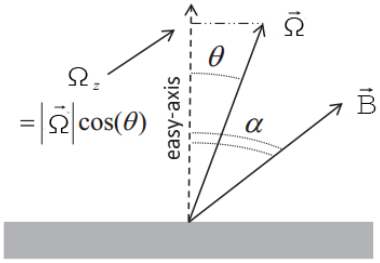

Figure 37: Illustration of the Anisotropy measurement setup. Figure adapted from [38]

$$E = K_z \sin^2(\theta) - \mu_0 M_s B \cos(\alpha - \theta), \tag{66}$$

is minimized. This criteria allows us to calculate K_z by means of doing a series of measurements varying the angle α and the strength B and then fitting to this dataset with fit parameter K_z. For larger values of α and large external magnetic fields, the Stoner-Wohlfarth theory is not valid anymore due to other effects in the ferromagnetic layer such as buckling. For our research, the fits are made to the datasets for values of $\alpha \leq 70°$. A typical dataset with fit is shown in figure 38.

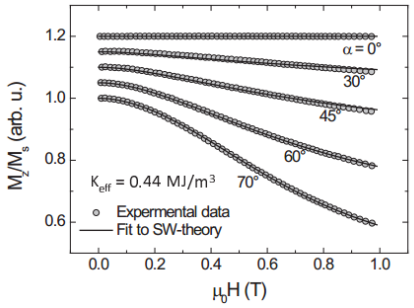

Figure 38: Dataset with fit from Stoner-Wohlfarth theory. Figure adapted from [38]

In the measurement, the strength of the anomalous Hall effect is measured by applying a current trough the sample in the plane of the external magnetic field and the easy axis and then measuring the voltage over the direction perpendicular to this plane. The results with their errors are listed and discussed in section 6.2.

Because the PMA for the samples arises due to interface effects between the ferromagnetic and nonferromagnetic layers, the PMA strength can give information about the interface structure. So for our experiment a variation of the anisotropy between the samples indicates a variation in the interface structure. As mentioned, we expect that for lower Ar gas flows the interface will be more rough and thus the anisotropy field will be lower because less interface area is aligned with the plane of the layers.

6.2 Results

For this experiment an array of samples has been made using sputter deposition. All samples are equivalent concerning the layer materials and thicknesses. The samples are denoted by $Ta(4nm)/Pt(4nm)/Co(0.6nm)/Pt(4nm)$. The difference between the samples is that when growing the last Pt layer the Ar gas flow has been varied from 2.1sccm (standard cubic centimeter per minute) to 40sccm which determines the Ar pressure during the deposition. The hypothesis is that a higher gas flow would cause the deposition to become less violent because the target atoms lose energy by collisions with the Ar gas, thereby making the interface between the Co and last Pt layer less rough. Since the DMI arises due to SIA [26], we would also expect a difference in DMI strengths for the different samples.

In an attempt to determine the strength of the DMI, we want to measure the DW velocity profile with respect to the IP magnetic field. If we observe a value B_0 around which the profile is mirror symmetric, we find the DMI strength $A_{DMI} = B_0 g\lambda$. So, using Kerr microscopy the velocity profiles have been determined for a set of samples where the Ar gas flow is varied between 2.1sccm and 10sccm. Also, to determine that indeed the interfaces are altered by the varying Ar gas flow, the anisotropy field of the samples has been measured, the total magnetic moment of the samples was determined and HRTEM images have been made to determine the interface roughness, degree of intermixing and interfaces structure respectively. During this process some interesting observations have been made. The interpretation and comparison with theory and literature will be done in section 7.

6.2.1 Expansion Shape

The first remarkable observation is that the shape of the domains changes when increasing the IP magnetic field. Also, for different gas flow rates different shapes are observed. The observations for two samples with Ar flow rates 2.1sccm and 10sccm are shown in figure 39. Notice that for the sample with the high gas flow becomes increasingly asymmetric by first taking on an egg-like shape at $B_x = 15$mT and then becoming more teardrop-like shaped at $B_x = 39$mT. However, the sample with the lower gas flow does not show this behavior, *i.e.* it takes on an elliptical shape and shows asymmetrical expansion, but not as extreme as for the high gas flow sample and the asymmetry does not further increase for increasing IP magnetic field.

Due to the current experimental setup, we only measure the DW velocities for one value of the OOP magnetic field per sample because we can only accurately observe velocities of the order $\sim 1\mu\text{ms}^{-1}$. However, it would be interesting to study if the shape also changes for different OOP magnetic fields, especially since the driving force is characterized by a domain whose width depends directly on the OOP magnetic field as explained in section

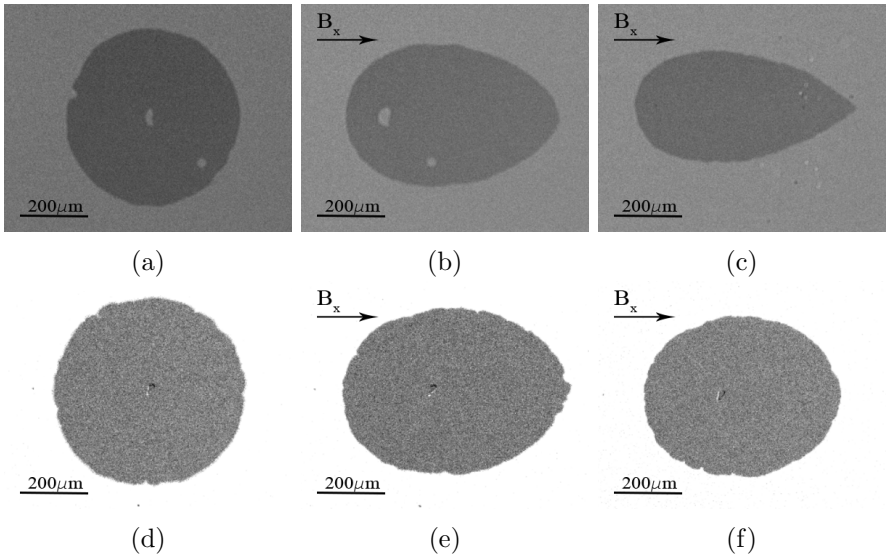

Figure 39: Kerr Microscopy images of DW expansion for two samples with Ar gas flow 10sccm (a-c) and 2.1sccm (d-f), with different IP magnetic fields. The spots in the center mark the nucleation points of the domain. (a,d) B_x = 0mT.(b,e) B_x = 15mT.(c,f) B_x = 39mT.

4.1.1. By use of OOP magnetic field pulses, it is possible to study the shapes and velocity profiles for higher OOP magnetic fields. At the time of the research for this Thesis, this setup was not available.

Another important observation is that the shape is slightly tilted with respect to the applied IP magnetic field as illustrated in figure 40, that is the horizontal axis of inversion symmetry for the shape has a nonzero angle with the direction of the IP magnetic field. This phenomenon might be just due to an experimental artefact, but it is also observed by other research groups [21].

6.2.2 Velocity Profiles

Figure 39 is taken from recordings of the DW expansion using the Kerr mircroscope. From these recordings datasets are formed by analyzing the DW position and time. Linear fits to these sets give us the DW velocity along a chosen direction. As mentioned in section 6.1, there might be leakage from the IP magnetic field to the OOP magnetic field (This of course also works the other way around, but because the OOP magnetic field is constant throughout the measurement series, this contribution will only give a constant offset). To account for this leakage we logarithmically average between the velocities of negative and positive domains. In figure 41 the velocity profiles for two samples with Ar gas flow 2.1sccm and 10sccm are shown for positive and negative domains.

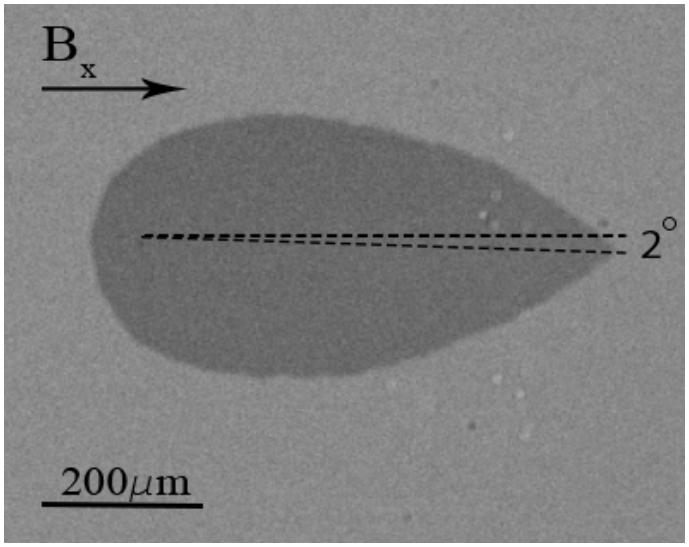

Figure 40: The shape of the expansion of a magnetic domain for one of our samples with an applied IP magnetic field. The symmetry axis appears to be slightly tilted with respect to the applied IP magnetic field.

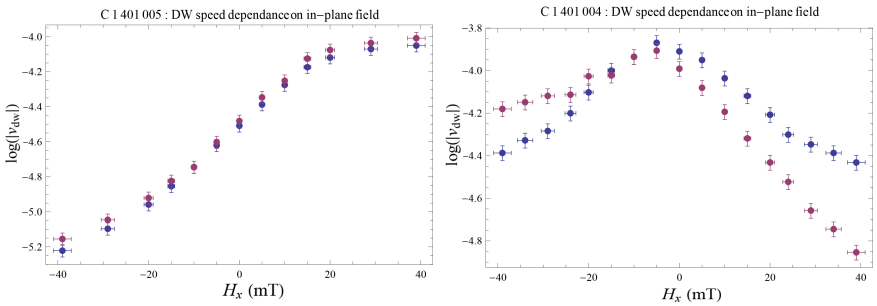

(a) (b)

Figure 41: DW velocity profiles for two samples with Ar gas flow 10sccm (a) and 2.1sccm (b). The blue dots mark the velocity profile for a positive domain and the purple dots mark a negative domain. The sample of figure (b) was not aligned perfectly with the setup. However by logarithmic averaging this can be compensated for.

This result is remarkable. To start with figure 41a, it looks like the DMI strength is just outside our measurement range and the velocity profile looks quite like the expected profile from the regular theory of creep as illustrated in figure 25b. However, if we try to fit such a curve from the theoretical model to this data set (see figure 42), we see that the measure profile flattens on the right hand side. As mentioned in section 4 this is something we intuitively expect to happen and also follows from the characterization of the driving force.

The second figure 41b is most interesting since it is nothing like the profiles expected from the regular theory. The result is reproducible and

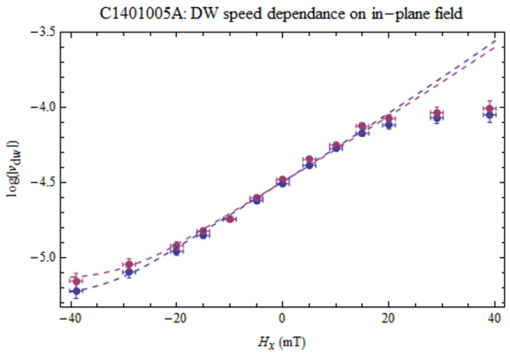

Figure 42: By fitting the regular theory of creep to our data, we observe that the profile flattens which is not explained by the theory.

shows approximately mirror symmetric behavior around $B_x = 0$. However, instead of having a minimum, it has a maximum.

If the exponent μ could take on negative values, this phenomenon could be explained to some extent by the regular theory of creep. However, $\mu < 0$ is not possible [31]. It would imply a finite DW speed when $B_z = 0$mT. Also our measurement of μ for this sample shows that its value is positive (see appendix B).

In figure 43 the result is shown of the entire measurement. Here, we study how the DW velocity profiles change for the different samples, by determination of the profiles for an array of samples grown with Ar gas flow ranging from 2.1sccm to 10sccm, compensating for leakage as mentioned above and scale the profiles on their OOP magnetic driving field via the suggested relation $\ln(v_{DW}) \propto -B_z^{-1/4}$.

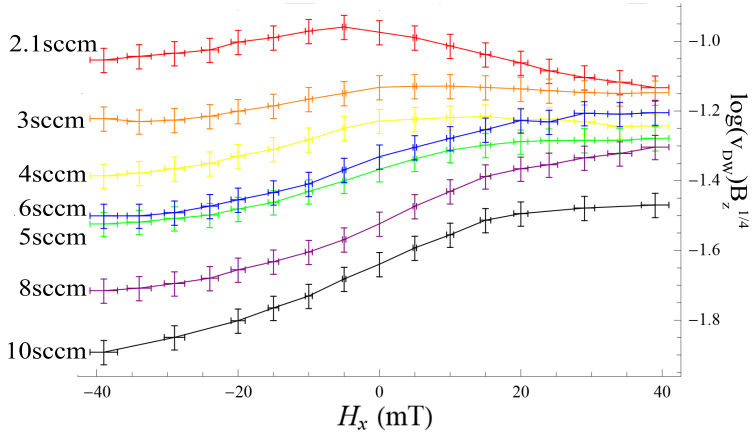

Figure 43: Scaled DW velocity profiles with respect to the IP magnetic field B_x for samples grown with Ar gas flow 2.1sccm (red), 3sccm (orange), 4sccm (yellow), 5sccm (green), 6sccm (blue), 8sccm (purple), 10sccm (black). It shows that the change from the profile in figure 41a to the profile from figure 41b seems to happen continuous.

The results show that the profile changes continuously and that for an Ar gas flow around 5sccm a maximum starts to form. In section 7 we further investigate this result, give a possible explanation and compare it with literature.

6.2.3 Anisotropy Measurement

To gain insight in the degree of interface roughness the anisotropy field for the samples has been determined using the Stoner-Wohlfarth theory.

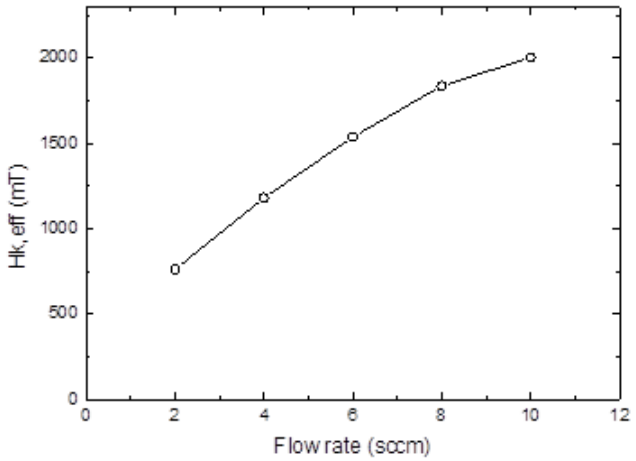

Figure 44: As expected we observe an increase of the effective anisotropy field with increasing Ar gas flow.

In figure 44 the results are shown. The results are in line with our expectation that the anisotropy increases for increasing Ar gas flow. One possible explanation, as also suggested in section 6.1.5, is that due to the higher gas flow, the interface is less rough and thereby more interface area is aligned with the plane of the layers. As explained in section 2.1.1, magnetic anisotropy arises due to effects on the interface with the easy axis perpendicular to the interface plane. So if we expect a smoother interface at higher Ar gas flows, we expect an increase of area aligned with the plane of the layers, thus an increase of PMA strength.

6.2.4 Magnetic Moment

When a nonmagnetic atom is embedded in a ferromagnetic material, a magnetic moment might be induced on the nonmagnetic atom. Thus a measurement of the total magnetic moment of the sample can give an indication of the degree of intermixing. The magnetic moment is determined with the VSM-SQUID setup for an array of samples with the same surface area (and

thereby the same volume of ferromagnetic material) grown with different Ar gas flows. The results are shown in figure 45.

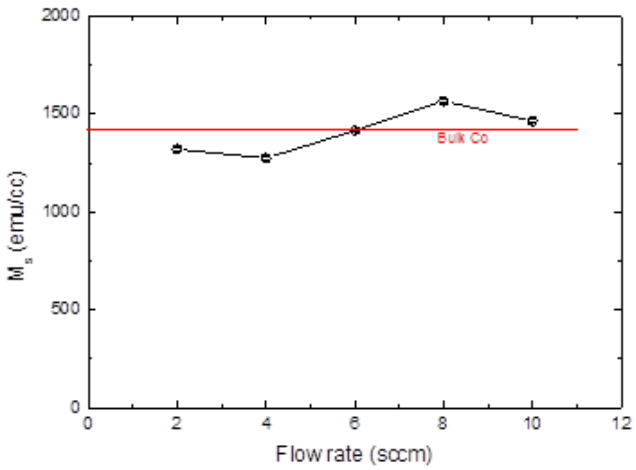

Figure 45: Measurement of the magnetic moment in units $emu/cc = 10^3 \mathrm{Am}^{-1}$ for samples with different Ar gas flows. The red line indicates the expected magnetic moment derived from the volume of ferromagnetic material.

An important remark to make here is that although the measurement of the magnetic moment is very accurate, hence the small errorbars, the calculation of the expected magnetic moment is less accurate due to the uncertainty of the layer thickness of the ferromagnetic layer. For a thickness of 0.6nm we expect that the layer consists of approximately 3 or 4 atoms. As already argued in section 3 the thickness can vary locally by approximately one lattice spacing distance, resulting in an error of $25 \sim 33\%$ locally.

Most measured magnetic moments lie close around the calculated magnetic moment. However, the sample grown with an Ar gas flow rate of 40sccm does seem to show a significant increase of magnetic moment. The question now arises if this is due to intermixing because we expected that for higher Ar gas flow rates the impacts of the deposited atoms are less violent, creating a smoother interface with less intermixing.

6.2.5 HRTEM Images

We conclude our experimental research by the study of HRTEM images of our samples. The imaging process and sample preparation is lengthy and expensive, so for this Thesis HRTEM images were only made for two samples grown with Ar gas flow rates of 2.1sccm and 10sccm. The images are shown in figure 46.

It is hard to distinguish between the different species of atoms, but the images do give insight in the lattice structure. The images emphasize that

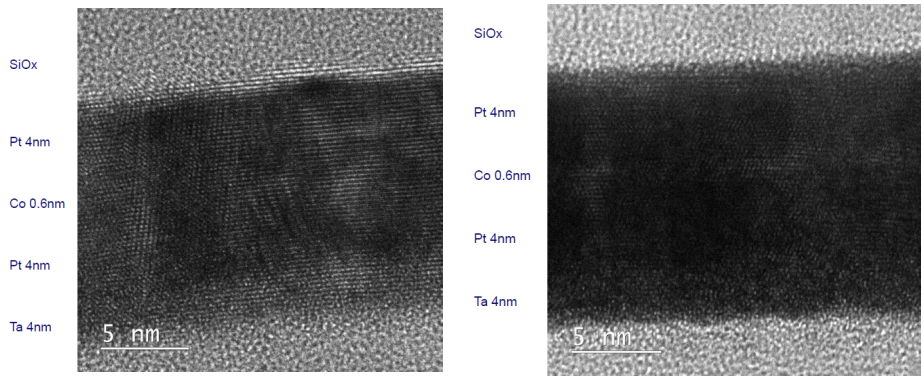

(a) (b)

Figure 46: HRTEM images for two samples with Ar gas flow 2.1sccm (a) and 10sccm (b).

the interface structure is not defined in a clear way. However, from these images no remarkable difference can be observed between the two samples. Other techniques need to be used to gain more insight in the structure of the sample. Here, our experiment meets the limit of current technology.

7 Interpretation and Comparison

Inthis Thesis numerous remarkable and interesting results have been obtained both theoretically and experimentally. Here we interpret and compare our experimental results, our theory and results to literature. First, we briefly consider the results from the fluctuating DMI theory. Then we elaborately treat the subject of creep theory with IP magnetic fields and DMI. Finally, we discuss the effect of varying growth parameters on the IP magnetic field dependence of the DW velocity.

7.1 Iridium and DMI Inversion

One interesting result from the theoretical discussion on fluctuating DMI is that DMI fluctuations enter the equation of motion for DWs as an effective IP magnetic field parallel to the DW. However, the fluctuation term $\partial_{r_{DW}} D_{DMI}$ can be negative, positive and zero and is very local, so this effective field is hard to observe and it is not yet feasible to set up an experiment to measure this local field. The theoretical discussion, combined with HRTEM images do imply that the DMI is not necessarily constant and may depend on the length scale of the DW width λ.

A result that does exhibits a connection with feasible experiment followed from the elementary study of interface profiles for the square lattice. As mentioned before, profiles such as the one illustrated in figure 21b allow for a negative energy contribution. One can also easily see that by making the peaks longer, the energy further decreases with -4ϵ per added atom.

Recent experimental research done by Hrabec *et al.* has shown that for samples with an Ir layer between the top Pt layer and the Co layer suggest that the sign of the DMI effect on the DW motion is reversed [21]. For this Thesis a similar sample was grown to see if we can reproduce this result. The measurement is described in appendix A. Our measurement also confirms the DMI contribution has switched from sign compared to samples without the Ir layer. The results of the measurement from the group of Hrabec *et al.* are shown in figure 47.

Clearly the inversion arises due to the introduction of a thick enough layer of Ir. This critical thickness is approximately the size of two atoms. One possible explanation for this phenomenon is that due to the Ir layer, interface structures like the one in figure 21b are formed. Increasing the Ir layer thickness would then result in a similar effect as adding more atoms to the peak. So for sufficiently thick Ir layers, the negative energy contribution from the top interface overcomes the positive contribution from the bottom interface and the total DMI effect on the DW motion is inversed.

This explanation is highly speculative and should be further investigated by imaging the true structure of the interface with for example HRTEM imaging. Also the theoretical models of interface profiles need to be further

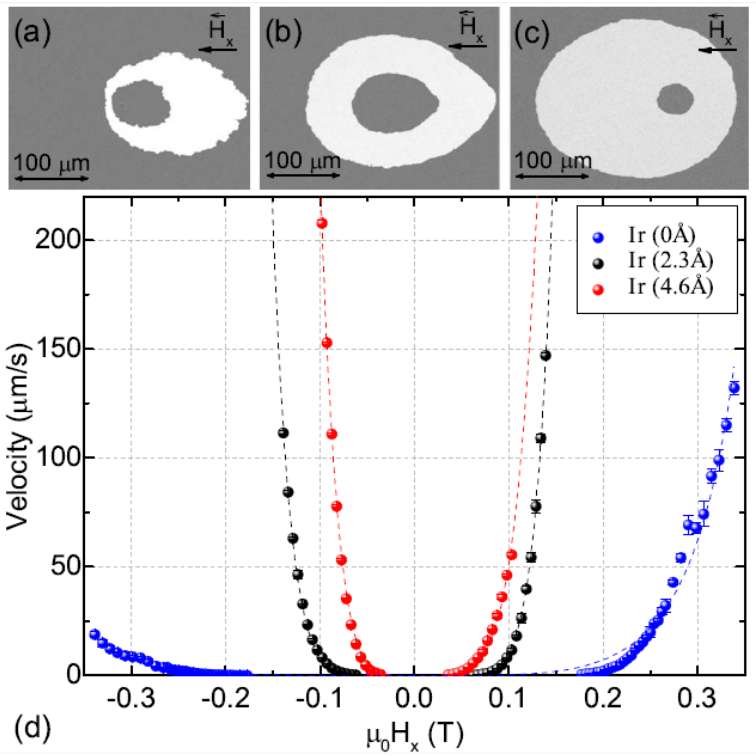

Figure 47: Experimental data from the research group of Hrabec *et al.* on samples with an Ir layer below the top Pt layer with varying thickness. (a-c) Kerr microscopy image of the three studied samples with the same applied IP magnetic field. The Ir layer thicknesses t are $t = 0$nm (a), $t = 0.23$nm and $t = 0.46$nm (c). (c) already shows the DMI effect has switched sign. (d) The data fitted to models from the regular creep theory. Figure taken from [21].

explored by studying more profiles for different lattice structures. This theory on interface effect could be used in micromagnetic simulation, making the interface roughness and lattice structure a simulation parameter to set the DMI.

7.2 IP Field Creep Theory

Our more controversial results regard the theory of creep combined with IP magnetic fields. First, the shapes of the expanding magnetic domain with an applied IP magnetic field, especially the egg-like and teardrop-like shapes, are not expected from the regular theory of creep as we see from the simulation in figure 31. In some literature it is suggested that the shape of the DW expansion remains circular, and the center of the circle shifts along the applied IP magnetic field [32]. In figure 48 their observation motivating this statement is shown.

Where the regular theory of creep does not predict nor explain the egg-

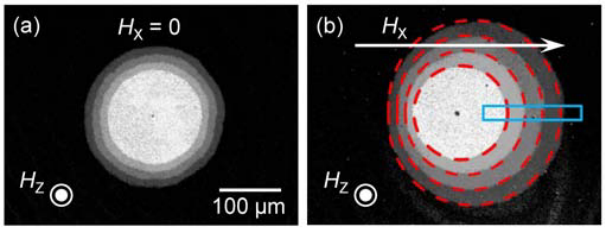

Figure 48: Observation of an expanding domain with an applied IP magnetic field $B_x = 0$mT (a) and $B_x = 50$mT (b). In both cases the expansion shape is circular. Figure taken from [32].

like and teardrop-like shapes, the suggested modification to the stiffness does give insight into why we observe this shape. Recall that the formula for the modified stiffness is

$$\tilde{\epsilon}_{el} = J_s - \frac{A_{DMI}^2 \pi \lambda}{2(A_{DMI} Q - g\lambda B_x)}. \tag{67}$$

Now, on one side of the expanding domain at the position of the DW the effective DMI field and the IP magnetic field align, *e.g.* in figure 39c that would be the right hand side, so the denominator of the second term in equation 67 becomes smaller, thus the second term itself becomes bigger, hence the total stiffness decreases due to the minus sign in front of the second term. On the other side, *e.g.* the left hand side, the effective DMI field and the IP magnetic field are anti parallel, resulting via the same reasoning in an increased stiffness. So at one side of the domain the DW becomes more elastic, whilst at the other side the DW becomes more stiff. This explains indeed the observed shape since on the side where the DMI field and IP magnetic field align, the DW makes a sharp bend, whilst at the other side the DW is near straight.

Another possible explanation comes from the same theory which we used to derive the stiffness modification in section 4.1.3. Recall that in equation 63 the second term corresponds to a tilting of the DW whenever an IP magnetic field, parallel to the DW is applied. When the parallel magnetic field B_y is positive, *i.e.* when $\hat{B}_y \times \hat{z} = \hat{x}$, the derivative $\partial_y X$ becomes negative. This follows from minimizing equation 63 with respect to $\partial_y X$ which is just a second order polynomial.

This results in a tilt of the DW in the counterclockwise direction. Analogously, if the parallel magnetic field is negative, the DW tilts clockwise. Now we approximate the shape of the domain by an n-sided polygon. For simplicity we take here $n = 4$ so we study a rectangle with two sides aligning with the IP magnetic field. For a positive IP magnetic field, the magnetic field at the bottom of the square is positive and parallel to the DW, so there the DW is tilted counterclockwise. On the top side the parallel magnetic field is negative, rotating the DW clockwise. On the left right hand side,

there is no component of the magnetic field parallel to the DW, so no tilting occurs there. The argument is illustrated in figure 49. The rectangular shape then indeed becomes more egg-like or teardrop-like shaped. Now by taking the limit $n \to \infty$ the argument applies to the real shape arguing that indeed the shape loses its vertical inversion symmetry. An inversion of the IP magnetic field also inverts the tilts and thus the shape, which we also observe in our experiment.

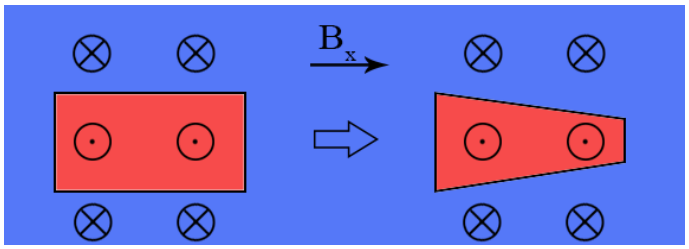

Figure 49: Transformation of a simplified, *i.e.* rectangular, magnetic domain shape, solely due to tilting.

Second, the slight tilt of the expansion shape is an interesting and reproducible phenomenon. The effect might occur just because of a misalignment of the camera and the magnetic coils. if this would be the case, then the tilt observed by inverting the IP magnetic field should be along the same line. This topic needs to be further investigated.

Third, the DW velocity profiles do not compare well with reports in literature and regular theory of creep. In section 5 we implemented the regular theory in 2D models of magnetic domain expansion and we can see that the shapes do not correspond for certain samples with nonzero IP magnetic fields. This has caused us to revisit the theory of creep, as done in section 4.

The three effects of the DMI and IP magnetic fields on the theory of creep we suggested, give us tools to better understand the velocity profiles. As we have seen, the characterization of the driving force also predict an offset in the profile due to the DMI and can be used to gain insight in why the flattening of the profiles occur. The effect on the energy density is already part of the regular theory of creep, but we argued that it is not the same effect as the driving force modification. Most insightful probably is the theory about the modification to the stiffness, which has already provided us with a way of understanding the expansion shapes. An important question to ask here is in what other ways the DMI and IP magnetic field can enter creep theory. As mentioned before, a good candidate is the DW width λ. How the DW width λ is affected by the IP magnetic field and the DMI should be further investigated.

The two most important observations from the DW velocity profiles are the flattening and the maximum for higher gas flows. As already men-

tioned, this flattening is not predicted by the regular theory of creep, but it does follow from intuitive arguments and our characterization of the driving force. This flattening can also function as a check for this driving force characterization because the characterization predicts a certain width of a domain outside which the flattening occurs. This width can be observed and the only parameters affecting it are the Gilbert damping parameter α_G and the applied OOP magnetic field B_z. An important remark to make here is that the value of B_x at which the egg-like domain expansion shape becomes teardrop-like, is also approximately the value where the velocity profile starts flattening.

The maximum in the DW velocity profiles, which occurs for the samples with lower Ar gas flows, is most controversial. In no way can the regular theory of creep allow for such a feature, thus this observation proves to be the largest motivation to rethink our current understanding of magnetic domain expansion and the theory of creep. However, once again, our suggested modification to the stiffness of the DW provides us with a way to understand this controversial phenomenon. In section 5.2.2 we implemented the stiffness modification in the theory of creep and illustrated its effect on the DW velocity profiles (see figure 32). Note that only the effect of the stiffness modification is shown, other effects are neglected. In figure 32b we see a maximum occurring at some value of B_x, larger than the effective DMI field. So here we at least have a theory where maxima are allowed.

To test if indeed this maximum occurs due to the stiffness modification, the velocity profile should be measured for a broader domain of IP magnetic fields. The theory predicts then that there is a minimum further to the left in this profile. If this speculative explanation would be valid, the question arises why we do not observe this maximum in the DW velocity profiles of samples grown with higher Ar gas flow rates. We suggest that for lower gas flow rates, the effect of the stiffness modification becomes more dominant. This dominance arises due to the fact that the amplitude of the modification to the stiffness scales with λ, which in turn scales with $1/\sqrt{K_z}$. As the anisotropy measurement described in section 6.2.3 shows, the anisotropy field decreases when the Ar gas flow rate lowers. Thus, the amplitude, which scales with $1/\sqrt{K_z}$ increases, making the stiffness modification more relevant for lower Ar gas flow rates.

7.3 Measuring the DMI

For the experiment, the original plan was to measure the DMI as a function of the Ar gas flow rate growth parameter. We expected to be able to determine the DMI by reading of the value of the minimum in the DW velocity profiles with respect to the IP magnetic field. As we have already elaborately discussed, these profiles do not correspond to the profiles expected from the regular theory [32]. We once again stress that before using the

theory as a method of measuring the DMI, which some research groups are already doing [21], the theory should be further investigated and revised.

Aside from the discussion on the legitimacy of the theory of creep, our experiment shows that the Ar gas flow growth parameter has a significant effect on the shape of expanding magnetic domains and on the DW velocity profiles with respect to the IP magnetic field. In literature often only the layer thicknesses of the samples are mentioned. We want to stress that sample growth parameters also influence the magnetic properties of the sample significantly.

8 Discussion, Conclusion and Outlook

To conclude this Thesis, we briefly discuss our methods and assumptions and then summarize the important results and conclusions that can be drawn from from our research, give an outlook on the implications of our results and suggest future research topics and studies.

To reflect back on our own work some important points of discussion need to be mentioned. First, the validity of the ansatz on the DW shape needs to be questioned. This ansatz is used throughout the theoretical work to derive models for the motion of magnetic domains and thereby has an important effect on our results. Also, the definition of our DW width λ follows from the DW shape which is derived from the Euler-Lagrange formalism applied on a simple Lagrangian density. However, the ansatz is reasonable for current or field driven systems, since the theory using this ansatz compares well to experiment [4, 5, 34]. The inclusion of IP magnetic fields might have an interesting effect on the definition of λ and the DW-shape and this should be investigated in future research.

Second, we want to stress once again that in this Thesis, the results derived from the LLG equation do not account for disorder potentials and therefore need to be interpreted as a speculative characterization of the true process. In future research this potential should be studied. This can easily be done by including a potential term in the derived equations of motion for the DW.

Third, in our theoretical work on the modifications to the creep theory we might not only overlook ways in which the IP magnetic field and DMI enter the theory, but we also might count certain effects double. The three suggested effect should not be regarded as disjoint, but as potentially overlapping parts of an unknown whole. One might wonder for example if the stiffness modification is (or should be) somehow included in the effect from the energy density.

As for our important results, from the theoretical work on Fluctuating DMI we have seen that local fluctuations in the DMI strength give rise to an effective IP magnetic field parallel to the DW. It would be interesting to setup an experiment where this effective IP magnetic field can be observed. However, due to the fact that the DMI fluctuations occur on a small length scale, this effective field is not constant throughout the material. However, if our understanding of the tunability of the DMI further develops, one might be able to make a sample with a fixed DMI gradient over the entire length of the sample. Then we should be able to observe the effective IP magnetic field due to the DMI variation.

More amenable to experimental research is the study of the effect of interface structures on the DMI. As we have elaborately discussed, it is possible to define certain interface structures where the total energy contribution of the DMI changes sign with respect to a perfect/straight interface structure.

This result is used to speculate about the origin of the phenomenon where indeed a DMI inversion is observed by the introduction of a thick enough Ir layer underneath the top Pt layer. To further investigate this speculation, the theory on interface structures should be broadened, not only accounting for square or hexagonal lattices, but also different types of lattices with imperfections. Relevant insight in the interface structures can also come from high resolution images of such samples, for example by use of HRTEM, energy dispersive X-ray spectroscopy mapping or atomic force microscopy.

The experiment done for for this Thesis and our theory on field driven creep theory show that the creep theory needs to be revised to form a more complete model of domain wall motion in PMA materials with IP magnetic fields. The series of measurements of our samples have shown shapes of the magnetic domain and DW velocity profiles that are not explained by the regular theory of creep. Our suggested modifications of the theory of creep do, to some extent, explain our observations and provide insight in the magnetic properties of the material and how they are affected by growth parameters. However, before setting up a more comprehensive theory of creep, these suggested modifications should be further investigated, inter alia, by measuring the DW velocity profiles over a larger domain. Also, we propose that the IP magnetic field and the DMI can affect the DW width λ, which plays an important role in the overal theory of the motion of magnetic domains.

An important conclusion that can be drawn here is that currently the theory has not developed far enough in order to measure the DMI strength of a sample. More insight is needed regarding the magnetic properties and processes of magnetic domains in PMA materials when an IP magnetic field is applied.

Also, the effect on magnetic properties of sample growth parameters, such as gas flow rates during the sputter deposition, on magnetic properties of the material appear to be quite significant. The DW velocity profiles change significantly by variation of the Ar gas flow when sputtering the top layer and also the anisotropy field increases significantly for higher gas flows. In this Thesis only the effect of the gas flow rate of Ar during the sputter deposition of the top Pt layer is studied. Future research can focus for example on the effect of temperature or the distance between the target and substrate during the sputter deposition. The effect of growth parameters can then be used to tune magnetic properties of the material such as the DMI.

The experiment done for this Thesis is of an exploratory nature. To fully comprehend the effect of varying the Ar gas flow during the sputter deposition of the top Pt layer, a lengthier series of measurements needs to be done, averaging over multiple different samples to cancel experimental errors, exploring a broader domain of IP magnetic fields and determining the DW velocity profiles for varying values of the OOP magnetic field to

further study the flattening and shape of the expanding domains.

9 Acknowledgements

First and foremost, I would like to thank my supervisors for guiding, helping and inspiring me throughout the research for my Thesis. You all seem to have survived my endless supply of questions and provided me with the right tools to find the answers. Rembert, it amazes me how you can come up with a theoretical concept within minutes, where I have to do calculations and crunch my brains for some days to arrive at the same conclusion. Erik, you have helped me a lot with keeping this research on the right track by assisting me with my scripts and calculations. Reinoud, you are the king of the laboratory not just by knowing how everything works, but also by knowing why it works and what theory underlies the process. Henk, you have motivated and inspired me with your ideas and straightforward questions.

Furthermore, this work is a collaboration between the Utrecht University and the Eindhoven University of Technology, motivated by the Science and Technology Eindhoven-Utrecht Strategic alliance. I am grateful for being able to make use of this strategic alliance. I also would like to thank everyonde from the Institute for Theoretical Physics at the Utrecht University and the Physics of Nanostructures group at the Eindhoven University of Technology for both scientific and social contributions.

References

[1] G.E. Moore, Electronics, **38**, 8 (1965)

[2] http://en.wikipedia.org/wiki/Moore%27s_law#mediaviewer/File:Transistor_Count_and_Moore%27s_Law_-_2011.svg

[3] S.S.P. Parkin, M. Hayashi, and L. Thomas, Science **320**, 5873 pp. 190-194 (2008)

[4] S. Emori, U. Bauer, S.-M. Ahn, E. Martinez, and G.S.D. Beach, Nature Materials **12**, 611-616 (2013)

[5] K.-S. Ryu, L. Thomas, S.-H. Yang, and S.S.P. Parkin, Nature Nanotechnology **8**, 527 (2013)

[6] A. Thiaville, S. Rohart, Ju, V. Cros, and A. Fert, Europhys. Lett. **100**, 57002 (2012)

[7] J.H. Franken, M. Herps, H.J.M. Swagten, and B. Koopmans, arXiv 1404.2945 (2014)

[8] K.-W. Kim, H.-W. Lee, K.-J. Lee, and M.D. Stiles, Phys. Rev. Lett. **111**, 216601 (2013)

[9] http://www2.technologyreview.com/article/412189/tr10-racetrack-memory/

[10] S. Lemerle, J. Ferr, C. Chappert, V. Mathet, T. Giamarchi, and P. Le Doussal, Phys. Rev. Lett. **80**, 4 (1998)

[11] P. Chauve, T. Giamarchi, and P. Le Doussal, Phys. Rev. B **62**, 6241 (2000)

[12] J. Ryu, S.-B. Choe, and H.-W. Lee, Phys. Rev. B **84**, 075469 (2011)

[13] K.-S. Ryu, L. Thomas, S.-H. Yang, and S.S.P. Parkin, Appl. Pys. Express **5**, 093006 (2012)

[14] D. J. Griffiths, *Introduction to Electrodynamics*, Pearson (2013)

[15] D. J. Griffiths, *Introduction to Quantum Mechanics*, Pearson (2005)

[16] H. Young, R. Freedman, F. Sears, and M. Zemansky, *University Physics with Modern Physics*, Pearson (2010)

[17] S.J. Blundell, and K.M. Blundell, *Concepts in Thermal Physics*, Oxford University Press(2010)

[18] L.D. Landau, and E.M. Lifschitz, *The Classical Theory of Fields*, Elsevier (1975)

[19] A. Aharoni,*Introduction to the Theory of Ferromagnetism*, Clarendon Press (1996)

[20] J. Stöhr, Journal of Magnetism and Magnetic Materials **200**, 470-497 (1999)

[21] A. Hrabec, N.a. Porter, A. Wells, M.J. Benitez Romero, G. Burnell, S. McVitie, D. McGrouther, T.A. Moore, and C.H. Marrows, arXiv 1402.5410 (2014)

[22] K.M.D. Hals, and A. Brataas, arXiv 1307.0395 (2013)

[23] http://www.science.uva.nl/research/cmp/qem/research_projects/

[24] I. Dzyaloshinkii, Journal of Phys. Chem. Solids **4**, 241 (1958)

[25] T. Moriya, Phys. Rev. Lett. **4**, 5 (1960)

[26] A. Fert, Phys. Rev. Lett. **44**, 23 (1980)

[27] F. Freimuth, S. Blügel, and Y. Mokrousovs, arXiv 1308.5983 (2013)

[28] R.A. Duine, *Spintronics*, Utrecht University (2010)

[29] P.J. Metaxas, J.P. Jamet, A. Mougin, M. Cormier, J. Ferré, V. Baltz, B. Rodmacq, B. Dieny, and R.L. Stamps, Phys. Rev. Lett. **99**, 217208 (2007)

[30] G. Blatter, M.V. Feigel'man, V.B. Geshkenbein, A.I. Larkin, and V.M. Vinokur, Rev. Mod. Phys **66** 1125 (1994)

[31] K.-J. Kim, J.-C. Lee, S.-M. Ahn, K.-S. Lee, C.-W. Lee, Y. J. Cho, S. Seo, K.-H Shin, S.-B. Choe, and H.-W. Lee, Nature **458**, 07874 (2009)

[32] S.-G. Je, D.-H. Kim, S.-C. Yoo, B.-C. Min, K.-J. Lee, and S.-B. Choe, Phys. Rev. B **88**, 214401 (2013)

[33] Information obtained from personal communication with the research group of Center for Subwavelength Optics and Department of Physics, Seoul National University, Seoul, Republic of Korea

[34] O. Boulle, S. Rohart, L.D. Buda-Prejbeanu, E. Jué, I.M. Miron, S. Pizzini, J. Vogel, G. Gaudin, and A. Thiaville, Phys. Rev. Lett. **111**, 217203 (2013)

[35] S. Bandiera, R.C. Sousa, B. Rodmacq, and B. Dieny, IEEE Magn. Lett. **2**, 3000504 (2011)

[36] J. Kerr, Philosophical Magazine **3**, 321 (1877)

[37] P. Weinberger, Philosophical Magazine Letters **88**, 897-907 (2008)

[38] R. Lavrijsen, *Another Spin in the Wall*, Eindhoven Univeristy of Tecnology (2010)

[39] M. Heide, G. Bihlmayer, and S. Blgel, Phys. Rev. B **78**, 140403(R) (2008)

[40] Schafer, *R. Handbook of Magnetism and Advanced Magnetic Materials*, vol. 3. Wiley (2007)

Appendix

A Reproduction of DMI inversion

An interesting phenomenon recently observed by Hrabec *et al.* is the inversion of the DMI effect in a sample with an Ir layer between the top Pt layer and the Co layer compared with a similar sample without the Ir layer [21]. In this Thesis it is suggested that this phenomenon might occur due to effects of the structure of the interface between the ferromagnetic and antiferromagnetic layer.

For this Thesis the DMI inversion phenomenon has been reproduced. We indeed observe a DMI inversion, which can be concluded just from imaging the shape of the expanding domain with an applied IP magnetic field. For positive DMI the DW moves faster along the direction of the IP magnetic field and slower in the antiparallel direction, as follows directly from the theory of creep. This speed difference is reversed when the DMI switches sign. As we can see from our own observation, the introduction of the Ir layer had indeed caused a negative DMI (see figure 50).

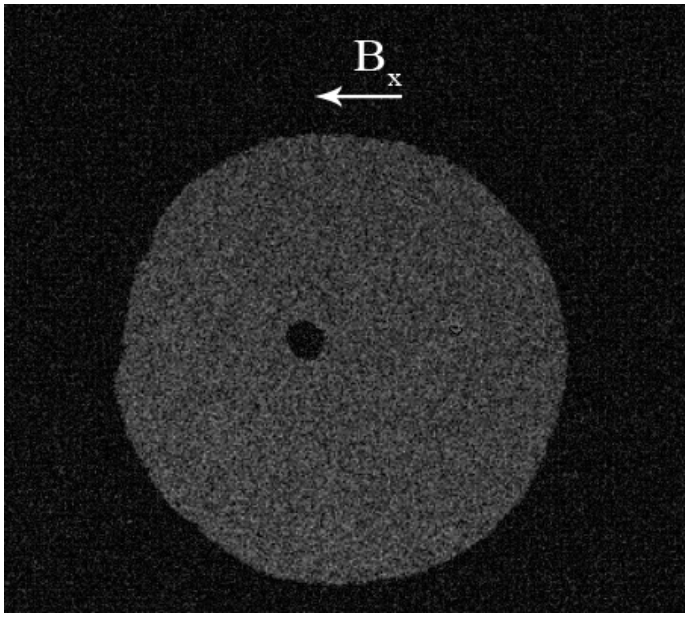

Figure 50: Expansion shape of a sample with an additional Ir layer between the top Pt layer and Co layer. The image is formed by subtracting two images at different times, thereby indicating the nucleation point with the dark spot inside the domain. The DM moves fastest in the direction antiparallel to the applied IP magnetic field, thus indicating a negative DMI.

B Measurement of Creep Exponent

In this Thesis we observed DW velocity profiles with respect to the IP magnetic field exhibiting a maximum. To only way a maximum can occur from the regular theory of creep is when the exponent μ becomes negative. This, however, would give us other complications, namely that the DW velocity is nonzero for zero OOP magnetic field which is physically not realistic. This consideration did provide an extra motivation to roughly measure the value of μ.

A second motivation came from the argument in the current theory of creep that the effect of the IP magnetic field on the driving force is in fact the same as the effect on the energy density because they occur in the exponent with the same power. However their powers are only the same is $(1-\mu)/3 = \mu$, thus if $\mu = 1/4$. By the definition of μ and the wandering exponent ζ, μ can be either 1 or 1/4. $\mu \neq 1/4$ would then lead to an interesting discussion. However, for our kind of samples μ has always found to be 1/4 [31].

The most relevant motivation comes from the data analysis used to determine the DW velocity profiles with respect to the IP magnetic field. As described, to compensate for leakage of the IP magnetic field to the OOP magnetic field, the DW velocities are measured for positive and negative domains. The two measured velocities at a given IP magnetic field then need to be averaged correctly. This can be done if we know how the DW velocity depends on the OOP magnetic field. The creep theory suggests $\ln v_{DW} \propto -B_z^{-\mu}$, so to properly average, we need to confirm that indeed the velocity of the DW scales exponentially with the OOP magnetic field and that μ equals 1/4. This can be done by fitting the the above relation to a dataset consisting of DW velocities at given OOP magnetic fields.

The data points and the fit result with fitted value and error of μ are shown in figure 51. It indeed shows that the velocity scales exponentially with the applied OOP magnetic field and that, within the error range, $\mu = 1/4$. This result can now be used to average correctly and compensate for leakage.

	Estimate	Standard Error	t-Statistic	P-Value
v0	9.52781	3.16251	3.01274	0.094771
α	4.02555	1.69707	2.37206	0.141069
μ	0.284828	0.0467852	6.08798	0.0259357

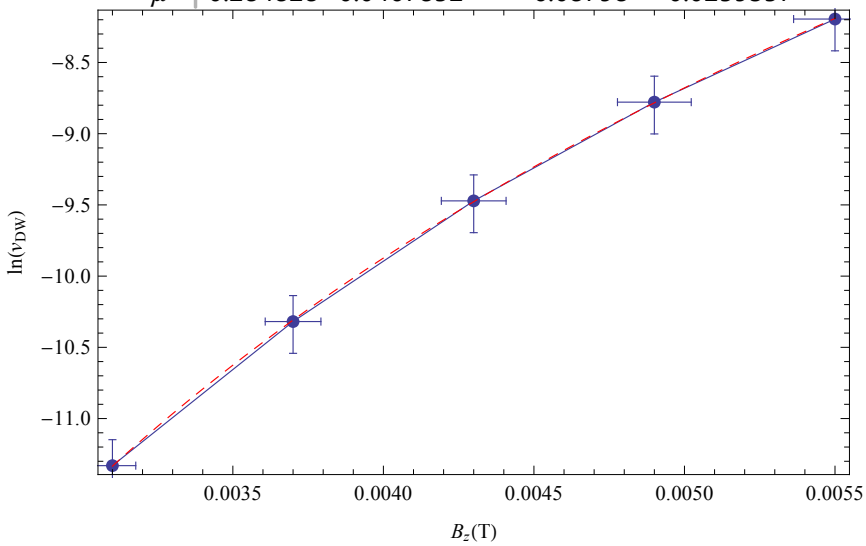

(a)

	Estimate	Standard Error	t-Statistic	P-Value
v0	22.6663	6.31366	3.59004	0.0695878
α	6.15377	3.15915	1.94792	0.190779
μ	0.28791	0.0551932	5.2164	0.0348408

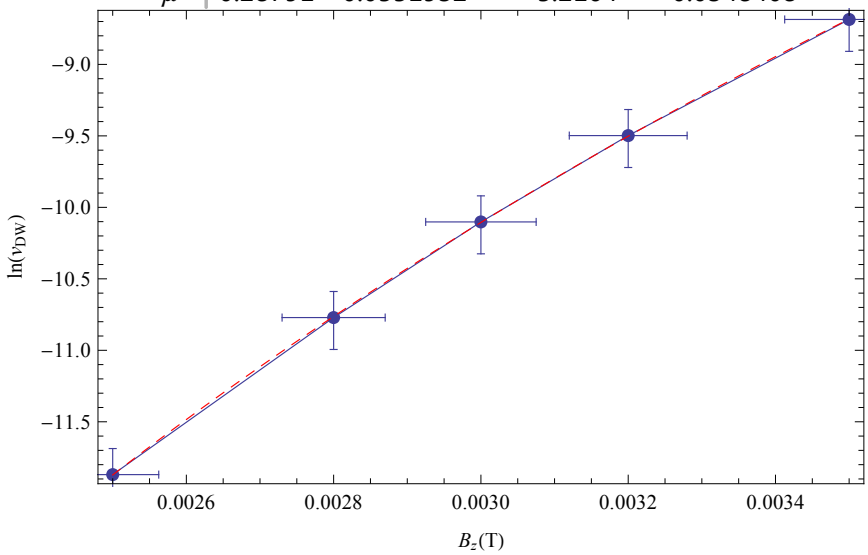

(b)

Figure 51: Measurement of the creep exponent μ by means of fitting $\ln(v_{DW}) = v_0 - B_z^{-\mu}$. The fit values and errors are shown in the tables above the graphs. The measurement has been done for two samples with Ar gas flow rate 2.1sccm (a) and 10sccm (b).